Investigating the Influence of Atmospheric CO_2, Bathymetry, and Salinity on Archean Ocean Circulation

Marissa M. Tripus

A Thesis submitted in partial fulfillment of

the requirements for the degree of

Master of Science

Atmospheric and Oceanic Sciences

at the

University of Wisconsin-Madison

June 2025

Thesis Declaration and Approval

I, Marissa M. Tripus, declare that this Thesis titled 'Investigating the Influence of Atmospheric CO_2, Bathymetry, and Salinity on Archean Ocean Circulation ' and the work presented in it are my own.

Marissa M. Tripus		
Author	Signature	Date

I hereby approve and recommend for acceptance this work in partial fulfillment of the requirements for the degree of Master of Science:

Hannah Zanowski		
Committee Chair	Signature	Date

Mayra Oyola-Merced		
Faculty Member	Signature	Date

Daniel Vimont		
Faculty Member	Signature	Date

Abstract

Investigating the Influence of Atmospheric CO_2, Bathymetry, and Salinity on Archean Ocean Circulation

by Marissa M. Tripus

During part of the Archean Eon (4 to 2.5 billion years ago), it is estimated that Earth experienced near-global ocean coverage. Little is known about the ocean during this time, but it coincides with—and may have been instrumental in—the earliest development of life on our planet. It is therefore essential to understand what the ocean's physical environment could have been within the early Archean Eon, as it can help us better understand the background under which life on our planet evolved. However, modeling this environment requires constraints on the atmospheric and oceanic conditions at the time, many of which span wide ranges (e.g., atmospheric CO_2 and other greenhouse gases, and ocean salinity) or have almost no constraints at all, such as ocean depth and bathymetry. Here we use the ROCKE-3D coupled atmosphere-ocean general circulation model configured for the early Archean environment to explore the ocean properties and circulation under a range of atmospheric and oceanographic parameters. Specifically, a suite of simulations is performed to understand how atmospheric CO_2 concentration, ocean salinity, and simplified ocean bathymetry could have impacted ocean circulation and heat transport. We find that 1) altering the atmospheric CO_2 concentration results in different ocean states ranging from cold, fully ice-covered, to warm, fully ice-free; 2) the addition of bathymetry leads to changes in both ocean density and the overturning circulation, but the strength of the changes depends on the specifics of the bathymetry; and 3) the influence of increased salinity is larger in a colder ocean with sea ice present compared to a warmer ocean with no sea ice.

Acknowledgements

First and foremost, I want to thank my advisor, Hannah, for taking a chance on me and this project. In 2022, when we had our first meeting, I knew this was the advisor I would want to work with. I was so excited when I received the offer to attend the University of Wisconsin-Madison with Hannah as my advisor. Throughout my first year, we took a large leap away from what we were both comfortable with, of modern and future Earth, to looking at past Earth to understand oceanography in a planetary framework. This had a steep learning curve, but I have enjoyed the journey. Thank you, Hannah, for being an amazing advisor over the past 3 years, and for always supporting me through the good and the bad.

To my committee, Mayra and Dan, I appreciate everything you have done for me. This ranges from providing input on my research, teaching me in courses, to helping me deal with personal struggles. To my friends from Millersville and Madison, thank you for the late-night conversations, the arguing over a term in a derivation, and for playing in the rain. I cannot imagine making it this far in my career without these unconditional friendships. There will always be a special place in my heart for the people on the 11th floor of the AOSS building.

To my family, thank you for never losing hope in what I am capable of achieving. From a very young age, I had very ambitious dreams of going into a STEM field. While we might not have had any idea of how things were going to unfold, you made sure to never let my dreams change. You pushed me to be the best version of myself. I would not be the person or scientist I am today without your unconditional love and support of my dreams. Thank you for everything.

Funding for this project was through the University of Wisconsin-Madison College of Letters & Science Advanced Opportunity Fellowship (AOF) under the Community of

Graduate Research Scholars (CGRS) program, the Wisconsin Alumni Research Foundation, and the Office of the Vice Chancellor for Research (OVCR) Research Forward program. I would also like to acknowledge the Center for High Throughput Computing (CHTC) at the University of Wisconsin-Madison for providing computational resources for this project.

Contents

List of Figures

List of Tables

Chapter 1

Introduction

1.1 Background

The Earth's climate has evolved drastically since our planet's formation over 4.5 billion years ago (Gya). The second eon on Earth, the Archean Eon (4 to 2.5 Gya), was the first time the planet semi-resembled modern Earth due to the presence of an ocean. Within the early eras of the Archean, the ocean is theorized to have formed via water delivery from asteroids and meteorites (Drake, 2005, Piani et al., 2023). The newly formed ocean likely encompassed the entire planet for much of the Archean, and by the end of the eon, Earth's surface was ∼7% land-covered (Albarede et al., 2020).

Despite the presence of a liquid water ocean, the environmental conditions of the Archean differed significantly from modern Earth. Moreover, planetary parameters were different too: the length of a day was ∼17 hours instead of the 24 hours we currently experience (Williams, 2000), and the solar luminosity was ∼75% of what it is today, which means the incoming solar radiation that Earth received was reduced by ∼25%. The decrease in solar luminosity occurred because the sun was much younger, so it did not radiate as intensely as it does today, therefore reducing how much radiation the planets around it receive. This is known as the faint young sun (FYS). The FYS largely contributed to the cold global temperatures throughout the Archean. When simulating the Archean with a modern Earth atmospheric composition, the global temperature estimates are below the freezing point of seawater until 3.5 Gya (Feulner, 2012). This suggests the early Archean eras would have experienced global glaciation. However, proxies do not support this (Blake et al., 2010, Feulner, 2012). When utilizing Archean proxies to derive an atmospheric composition, the global temperatures increase outside of the range for global glaciation (Feulner, 2012), an apparent mismatch commonly referred to as the FYS paradox. This work, and others, suggest that the FYS, which acted to cool the planet, was most likely counteracted by other environmental parameters, such as greenhouse gas concentrations (Feulner, 2012, Sagan and Mullen, 1972).

The environmental parameters of the Archean are challenging to study due to the Earth's high level of geological activity throughout its history. The past 4 billion years of seafloor movement have left limited sediment and rock records available for analysis. Consequently, there are large ranges of variability for atmospheric and oceanic parameters. Some examples are: CH_4 is estimated to be 100x – 10,000x present level (PL) (Zahnle et al., 2006, 2019), CO_2 is estimated to be 10x – 2,500x PL (Driese et al., 2011, Farquhar et al., 2011), ocean salinity is estimated to be 20 to 50 g kg^{-1} ($\pm$ 15 g kg^{-1} from PL) (Marty et al., 2018), and many more.

Early research on the Archean was performed via lab work or simplified 1-dimensional models, but in recent years, general circulation models (GCMs) have been used to further explore the eon. Some of the earliest Archean GCM studies were conducted to address the FYS paradox (Charnay et al., 2013, Wolf and Toon, 2013, 2014). Through these various modeling projects, several theories have been created to address why the planet was not glaciated and had a climate similar to modern Earth. These theories include clouds and planetary albedo (Charnay et al., 2013), an abundance of greenhouse gases (primarily CO_2 and CH_4) (Charnay et al., 2013, Wolf and Toon, 2014), and Earth's faster rotation rate (Wolf and Toon, 2014). Another approach explored the role of ocean salinity in the climate system of Archean Earth, and how it helped enhance or inhibit the presence of sea ice (Olson et al., 2022). The results showed that the more saline the ocean is, the warmer the climate will be. Therefore, salinity itself could also help reduce the effects of the FYS (Olson et al., 2022).

Outside of Olson's recent work (Olson et al., 2022), an important caveat that arises in most of these studies is that they do not account for ocean dynamics and circulation, as Olson et al. (2022) uses a fully-coupled atmosphere-ocean GCM (modeling a full-depth dynamical ocean). For example, Charnay et al. (2013) uses an atmospheric GCM coupled to a two-layer ocean model (modeling a surface mixed layer and deep ocean layer, capturing the mean wind-driven circulation and transport heat) and various land distributions (i.e., modern continents, supercontinent, and no continents/land), and Wolf and Toon (2013, 2014) use an atmospheric GCM coupled to a mixed-layer ocean (modeling only the upper ocean, capturing surface processes) and a modern Earth land distribution. Although these are good assumptions within the context of each study, they are not fully representative of the Archean environment because they neglect the roles of ocean circulation and atmosphere-ocean coupling in setting the climate of this eon. These studies also did not focus on the impact of land-sea distribution on the ocean because they focused primarily on how the atmosphere could counteract the FYS. As more research is done, estimates of the Archean land cover amount and distribution change, making it hard to create the 'most realistic' land distribution within any given simulation (Albarede et al., 2020, Charnay et al., 2013). Although Olson et al. (2022) did not include any land in their simulations, their fully coupled atmosphere-ocean framework still renders their simulations some of the most representative of the Archean climate system thus far.

It is well-established that the presence or absence of land boundaries can impact oceanic and atmospheric heat transport and circulation, leading to major changes in the climate system (e.g., Enderton and Marshall, 2009, Marshall et al., 2007, Smith et al., 2006, Wu et al., 2021). The same is implied for the presence or absence of ocean bathymetry, as adding or removing a single bathymetric feature in a simulation can change the ocean circulation and heat transport by $\pm$ 0.2 PW (Gille et al., 2004). Yet Olson's simulations, in addition to most traditional aquaplanet studies (including those above), are run with a flat-bottom ocean of uniform depth. Although a flat-bottom ocean yields a simplified framework for understanding the influence of land boundaries on ocean circulation, it is unlikely that the Archean's ocean was flat because the Earth was already tectonically active at this time (Brown et al., 2020, Ernst, 2009, Kuzmin et al., 2016). Additionally, given that there may not have been significant land masses present for most of the Archean, ocean bathymetry, rather than land, would thus be the major contributor to topographic steering, mixing, and vertical exchange.

1.2 Research Questions

While we know the Archean climate was much different from our planet's climate today, very few studies have attempted to understand the basic physical oceanography of this time, particularly ocean circulation and heat transport. Understanding the ocean's physical environment in the early Archean can provide insight into the habitability of early Earth. The earliest life developments on Earth occurred within the Archean Eon, most likely in the ocean (Lepot, 2020). Therefore, by studying the role of the ocean circulation in Archean Earth's climate, the additional understanding that we gain could help us better constrain the conditions in which life evolved on our planet.

To this end, the presented work in this thesis explores ocean circulation, properties, and heat transport during the early Archean Eon using a fully coupled atmosphere-ocean aquaplanet GCM. The definition of an aquaplanet utilized in this thesis is: a planet with a surface entirely comprised of water (i.e., all land is removed) with a dynamical atmosphere and dynamical ocean. In the context of their impacts on ocean properties and dynamics, three specific atmospheric and oceanic parameters will be analyzed: atmospheric CO_2

concentration, ocean bathymetry, and ocean salinity. The major scientific questions that will be addressed in this project are the following:

Question 1: How does the concentration of atmospheric CO_2 alter Archean ocean properties and circulation?

Question 2: How does the addition of bathymetry change the Archean ocean's properties and circulation?

Question 3: How does increasing the ocean salinity change the Archean ocean's properties and circulation?

1.2.1 Influence of Atmospheric CO_2

Throughout Earth's history, the concentration of atmospheric CO_2 has varied significantly, with large impacts on the overall climate state. As stated earlier, the possible CO_2 levels during the Archean span a large range. Testing two CO_2 levels (a low and a high) allows us to capture the extreme ends of what the Archean climate potentially was.

Olson et al. (2022) previously tested the influence of atmospheric CO_2 on the climate state, but only focused on sea ice coverage when discussing the ocean. Their findings show an inverse relationship between the atmospheric CO_2 and sea ice coverage; as atmospheric CO_2 increases, the sea ice coverage decreases (Olson et al., 2022). In addition, as the atmospheric CO_2 increases, the global temperature increases (Olson et al., 2022). The analysis in later sections of this thesis will discuss the impacts of atmospheric CO_2 on the ocean state, in addition to the sea ice coverage.

1.2.2 Influence of Bathymetry

The ocean's bathymetry, or seafloor topography, plays a critical role in ocean circulation and heat transport. It helps to steer the water's flow, and it also enhances or inhibits the mixing and transport of different water masses (Gille et al., 2004). This has been investigated on modern Earth and within aquaplanets (i.e., Enderton and Marshall, 2009, Mercier et al., 2000, Smith et al., 2006, Wu et al., 2021). A prime example on modern Earth is the Mid-Atlantic Ridge, which acts as a barrier between the water masses of the eastern and western Atlantic Ocean (Mercier et al., 2000). As others have tested and shown how various land distributions influence the ocean (i.e., Enderton and Marshall, 2009, Mercier et al., 2000, Smith et al., 2006, Wu et al., 2021), we test how much influence various bathymetric configurations have on the global ocean circulation, property distributions, and heat transport. The analysis in later sections will discuss these effects.

1.2.3 Influence of Salinity

Ocean salinity plays a critical role in seawater's density, along with temperature and pressure. Cullum et al. (2016) shows that in oceans with extremely high salinity (260 g kg^{-1}), the meridional overturning circulation (MOC) can reverse, leading to upwelling in the polar regions, downwelling in the equatorial regions. This is the opposite behavior of what we see on modern Earth. Although it is unlikely the Archean's ocean reached such a high salinity, testing two salinities (low and high) within the plausible salinity range of the Archean can help us understand the role of salinity in the ocean's circulation. The analysis in later sections will discuss the influence of ocean salinity on ocean properties, circulation, and sea ice coverage, as we expect to see changes in these spatial patterns from the Cullum et al. (2016) paper.

Chapter 2

Methods

2.1 Model

We use the Resolving Orbital and Climate Keys of Earth and Extraterrestrial Environments with Dynamics (ROCKE-3D) three-dimensional atmosphere-ocean GCM, developed at NASA Goddard Institute for Space Studies (GISS) (Way et al., 2017), to model the early Archean. ROCKE-3D was designed for planetary and deep-time paleoclimate studies (Way et al., 2017), hence making this model ideal to use when modeling an Archean aquaplanet. ROCKE-3D includes an atmosphere component, an ocean component, a thermodynamic sea ice component, various radiation schemes, reduced chemistry, and no geothermal heating. ROCKE-3D has a horizontal resolution of 4° latitude x 5° longitude in all components (Way et al., 2017). The vertical component of the atmosphere has 40 layers (~60 km in altitude, or 0.1 hPa at the top of the atmosphere), and the vertical component of the ocean has 13 layers (maximum depth of 4,647 m) (Way et al., 2017). Ocean mesoscale eddies are represented by a Redi/Gent-McWilliams scheme (Way et al., 2017). When using ROCKE-3D for aquaplanet simulations, the model requires land at the South Pole as a technical limitation.

2.2 Simulations

The model configuration is modified from Olson et al. (2022). The following parameters are changed from modern Earth values (Table 2.1: rotation rate, atmospheric chemical composition, incoming solar radiation, atmospheric pressure, and ocean salinity. The changes to these parameters are based on multiple paleoclimate studies: the rotational period is 17 hours (Williams, 2000); the incoming solar radiation is set to 1029.37 W m^{-2}, (25% of modern; Gough, 1981); the total atmospheric pressure is 0.5 bar (Som et al., 2016); the obliquity is set to 23.5°, and eccentricity is set to 0°. For the atmospheric constituents (relative to modern levels), O_2 (Zahnle et al., 2006) is set to zero, atmospheric CH_4 is 1,000 times higher (Kasting, 2005), atmospheric CO_2 is 10 times higher ('low' CO_2 case; Driese et al., 2011) or 500 times higher ('high' atmospheric CO_2 case). The ocean is set to a mean depth of 1,360 m (10 layers), and various bathymetries (detailed below) are applied. Two ocean salinities are also tested: 'low' salinity (35 psu) and 'high' salinity (50 psu). The low CO_2 concentration was selected to follow Olson et al. (2022) model set up, while the high CO_2 concentration was selected as this is the level of

CO_2 at which sea ice stops forming on the planet. All other parameters are assumed to be modern Earth values.

The 10-layer ocean can reproduce key aspects of the modern ocean's overturning circulation, including sinking dense water at high latitudes. Olson et al. (2022) briefly discusses this and includes supplementary figures showing the overturning of a simulated modern ocean with 10 layers instead of 13 layers.

Four bathymetries are simulated to investigate the influence of bathymetry on the ocean. These bathymetries are Flat, Ridge, Rough, and Ridge + Rough (Figure 2.1). All configurations have a maximum ocean depth of 1,360 m. Flat has a uniform ocean depth. Ridge has a similar aspect ratio to a modern mid-ocean ridge (peak at 650 m and ~1,000 km wide). Rough has randomly distributed bathymetric features in size and location across the seafloor to simulate seamounts and abyssal hills (maximum peak at 1,020 m, keeping similar height to modern oceanic features). Ridge + Rough is a combination of the Ridge and the Rough bathymetric features. We do not expect other similar random distributions of bathymetry to yield large differences in the results.

A total of eight simulations are discussed within this thesis (Table 2.2). There are four flat ocean runs that isolate the impact of changing atmospheric CO_2 and/or changing ocean salinity, and an additional four runs that isolate the impact of changing bathymetry in both the high and low atmospheric CO_2 cases. In the low atmospheric CO_2 case, all four bathymetries (Figure 2.1) are simulated. These are Flat 10x (F10), Ridge 10x (Ri10), Rough 10x (Ro10), and Ridge + Rough 10x (RR10). In the high CO_2 case, only the Flat

(F500) and Ridge + Rough (RR500) bathymetries are simulated due to redundancy in some of the results (see Section 3.2.2). The two flat ocean cases, F10 and F500, are used to isolate the impacts of changing atmospheric CO_2 on the ocean. F10 and F500 also have high salinity counterparts in which their salinities are increased from 35 psu to 50 psu. These are Flat 10x-50 psu (F10-50) and Flat 500x-50 psu (F500-50). These simulations are used to explore the impact of changing salinity in both of the atmospheric CO_2 cases.

All simulations are initialized from an ice-free state. Each simulation takes 1,000 to 3,000 years of model time to achieve steady-state (depending on the atmospheric CO_2 levels). Steady-state is defined as the mean global deep ocean temperature experiencing a drift of less than a hundredth of a degree Celsius (< 0.01°C). All analysis is done using an average of the last decade of each simulation.

2.3 Analyses

The following parameters are analyzed for each simulation: sea ice coverage (%), zonal ocean potential density (sigma notation ($\sigma = \rho(S, \vartheta, 0) - 1,000)$); kg m^{-3}), meridional oceanic heat transport (OHT) (PW), and oceanic meridional overturning circulation (MOC) streamfunction (Sv). Of these, the sea ice coverage and MOC are direct outputs from the model. The zonal ocean potential density is the ocean potential density averaged over all longitudes to produce the zonal mean. The OHT is calculated as OHT = $\rho\ c_p\ \vartheta\ v$, where ρ is the ocean density, c_p is the heat capacity of seawater, ϑ is the ocean potential temperature, and v is the meridional velocity, and then integrated over depth and longitude to achieve the total ocean meridional OHT.

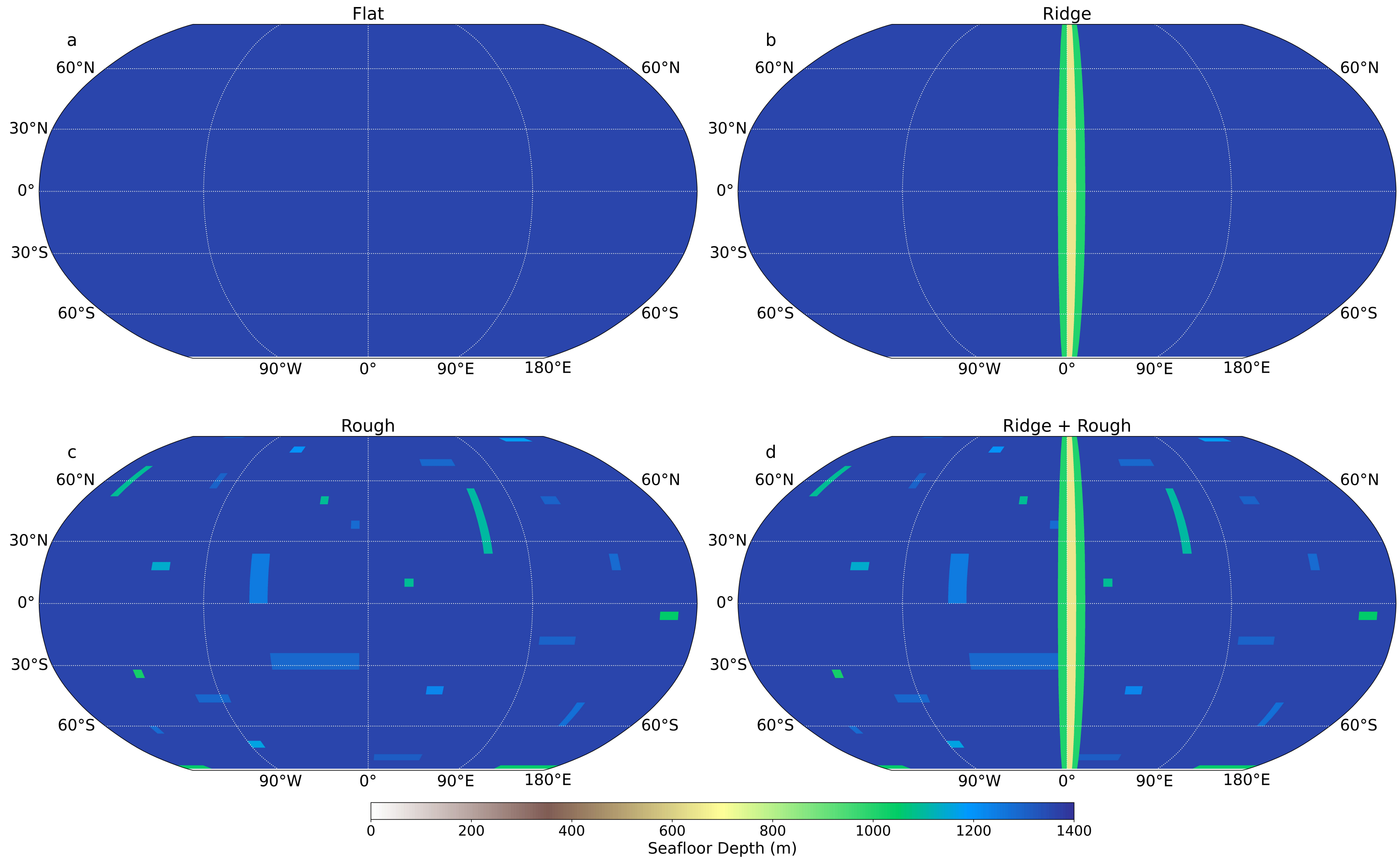

FIGURE 2.1: The four bathymetry configurations used in the simulations. All have the deepest ocean floor at 1,360 m. The plots are as follows: (a) Flat, (b) Ridge, (c) Rough, (d) Ridge + Rough.

Parameter	**Values**	**References**
Day Length	17 hr	Williams (2000)
Insolation	1029.37 W m^{-2}	Gough (1981)
Total Atmospheric Pressure	0.5 bar	Som et al. (2016)
Obliquity	23.5°	-
Eccentricity	0°	-
CH_4	1,000x PL	Kasting (2005)
CO_2	10x PL 500x PL	Driese et al. (2011) -
O_2	0	Zahnle et al. (2006)
Ocean Depth	1,360 m	-
Salinity	35 psu 50 psu	Marty et al. (2018) Marty et al. (2018)
Land Configuration	Aquaplanet	Albarede et al. (2020)
Bathymetry	Flat, Ridge, Rough, Ridge + Rough	-

Table 2.1: Summary of model configurations. Not mentioned parameters are assumed to be the same as those of modern Earth.

Simulation	**Abbreviation**	**Parameters**
Flat 10x	F10	Flat, 10x PL CO_2, 35 psu
Flat 500x	F500	Flat, 500x PL CO_2, 35 psu
Ridge 10x	Ri10	Ridge, 10x PL CO_2, 35 psu
Rough 10x	Ro10	Rough, 10x PL CO_2, 35 psu
Ridge + Rough 10x	RR10	Ridge + Rough, 10x PL CO_2, 35 psu
Ridge + Rough 500x	RR500	Ridge + Rough, 500x PL CO_2, 35 psu
Flat 10x 50 psu	F10-50	Flat, 10x PL CO_2, 50 psu
Flat 500x 50 psu	F500-50	Flat, 500x PL CO_2, 50 psu

Table 2.2: Summary of model simulations. In 'Parameters', the parameters are listed as follows: bathymetric configuration (Figure 2.1), CO_2 concentration, and average salinity.

Chapter 3

Results

3.1 Influence of Atmospheric CO_2

The two atmospheric CO_2 concentrations (10x PL and 500x PL) with flat-bottom ocean simulations yield different ocean states. F10 is an ice-covered Earth (sea ice thickness ranges from 9 to 143 m, with a global average of 29.8 m), while F500 is an ice-free Earth (Figure 3.1). The average global surface air temperatures of -48°C for F10 and 33°C for F500 influence the sea ice coverage. The density structure, OHT magnitudes, and MOC magnitudes and structures are also different.

The zonal mean potential density structure of F10 resembles what we see on modern Earth. This structure consists of less dense water in the equatorial region, a rapid transition to denser water (at $\sim$35°N/S within the model simulation), and the densest water in the polar regions, creating a bowl-like structure (Figure 3.2a). While this shape reflects the ocean dynamics and thermodynamics, we can investigate the ocean's potential temperature and salinity to see their impacts on the density, based on the ocean's equation of state. Both the potential temperature and salinity follow similar spatial distributions to the density (Figure 3.2c-f). The zonal potential temperature ranges from -2.1 to -1.7°C (Figure 3.2e), and the zonal salinity ranges from 30 to 39 psu (Figure 3.2c) throughout the ocean. From these, in F10, the lower latitudes have warmer and fresher water, leading to a lower density region. In comparison, the higher latitudes have colder and saltier water, leading to a higher density region. The ocean itself is also very cold, with temperatures around freezing throughout, reflecting the very cold atmospheric state and global ice coverage.

In F500, the ocean is overall much warmer than in F10, with all temperatures above freezing, owing to the warmer climate state due to the increased CO_2 concentration. The zonal mean potential density structure of F500 experiences a reversal from what we see in F10. There are higher densities in the equatorial region and lighter densities in the polar regions, with an overall decrease in the ocean's density (Figure 3.2b). The zonal potential temperature ranges from 5 to 40°C (Figure 3.2f), and the zonal salinity ranges from 31 to 45 psu (Figure 3.2d) throughout the ocean. At low latitudes, the ocean is warmer and saltier with higher densities, and at high latitudes, the ocean is colder and fresher with lower densities. Given these relationships, salinity has a larger impact on the density values in both of these regions for F500. Another feature of the F500 density structure is a spike of high density at 25°N (Figure 3.2b). The density spike is co-located with an area of very high surface evaporation (not shown). This strong evaporation leaves the ocean more saline at 25°N, creating a region of strong downwelling and also contributing to the high density values at this location.

The salinity between F10 and F500 is largely different, with F10 having a global average salinity of 34.55 psu, and F500's average is 40.56 psu (a 17% increase from F10). Early analysis of the salinity increase is suggested to be linked to the amount of water in the ocean. In both the mass of the ocean and the sea surface height (SSH) (both not shown), there is a 17% reduction in values. The ocean lost ~240 m of water, but the salt stayed in the ocean, leading to a global increase in salinity. Further analysis is required to understand where all of this water has gone, as it is not reflected in the atmospheric water vapor.

The MOC of F10 consists of one overturning cell per hemisphere spanning the full depth of the ocean. The orientation of the circulation is such that there is upwelling along the equator, poleward motion at the surface, downwelling at high latitudes, and equatorward motion at depth (Figure 3.3c), similar to what we see on modern Earth. Each cell has two regions of stronger MOC peaking at ~4.5 Sv, and reaches 50°N/S. The structure of the MOC is largely attributed to the density structure, as the densities influence where there is rising and sinking water. In addition, the MOC is influenced by weak meridional currents within the ocean (peaking at 1.7 cm s^{-1} at the surface and 1.0 cm s^{-1} at 1,130 m). In this simulation, there are no boundaries within the ocean, creating a very zonal pattern within the currents, rather than the horizontal gyre-like pattern like we see in the wind-driven surface currents on modern Earth, hence, the contribution of meridional currents is reduced. F10 experiences poleward OHT in both hemispheres, following the meridional temperature gradients set by the distribution of incoming solar radiation and the general structure of the MOC. The OHT peaks at ∼1 PW at 25°N (Figure 3.3a), while on modern Earth, the OHT peaks at 2 PW at 20°N (Trenberth and Caron, 2001). The reduced OHT is likely a combination of the overall colder ocean of F10, the reduced meridional temperature gradient in the ocean (-2.1 to -1.7°C), and the reduced MOC. This weak OHT is also reflected in the global average net heat into the ocean being -0.000186 W m^{-2}.

F500's MOC has one strong cell sitting on the equator spanning 25°N/S, and a weaker cell confined to 25 to 45°N. The MOC streamfunction peaks at ∼70 Sv in the equatorial region, which is an order of magnitude stronger than F10. There is a reversal of the MOC relative to F10 (and that of modern Earth). At 25°N, high surface evaporation (discussed earlier) brings about high surface salinity and an increase in density that leads to strong downwelling, which makes up the northern limb of the main overturning cell. The water then moves southward until 25°S, upwells to the surface, and then moves northward (Figure 3.3d). The currents are still predominantly zonal, like in F10, but the meridional currents are stronger at the surface, peaking at 5.3 cm s^{-1} at the surface and 0.12 cm s^{-1} at 1,130 m. The surface meridional currents are stronger in F500 because the wind stress can directly impact the ocean when no sea ice is present (i.e., Brenner et al., 2021, Muilwijk et al., 2024). The OHT is northward from 90°S to 25°N, and southward from 25 to 90°N, following the MOC. The OHT peaks at ∼6 PW at 10°N (Figure 3.3b), which is triple the maximum on modern Earth (Trenberth and Caron, 2001) and 6 times that of F10. The increase in the OHT is attributed to the overall ocean being warmer, the larger meridional temperature gradient (5 to 40°C), and the increased current speeds that factor into the MOC. The increase in OHT in F500, compared to F10, is also reflected in the global average net heat into the ocean being -0.331 W m^{-2}, which is three orders of magnitude stronger than the net heat into the ocean of F10. Thus, highlighting how the presence of the sea ice in F10 largely dampens the heat exchanges of the ocean and atmosphere, as well as dampens the OHT on the planet. This finding occurs in all presented ice-covered and ice-free simulations.

3.2 Influence of Bathymetry

In the previous section, a flat-bottom ocean was investigated, however, this section analyses the influence of adding bathymetric features (i.e., a ridge, seamounts, and abyssal hills) to create simplified seafloor topographies. The density structure, MOC, and OHT are analyzed for all four bathyemetries at 10x CO_2, while only Flat and Ridge + Rough are analyzed at 500x CO_2. These parameters are compared at each CO_2 concentration to understand the isolated impacts of the bathymetry. Moreover, these changes are compared across the low and high CO_2 concentrations to gain insight into how the results vary in different ocean states.

3.2.1 10x CO_2

The four bathymetries, Flat, Ridge, Rough, and Ridge + Rough, all yield similar results for the sea ice coverage (not shown) and zonal mean potential density in the 10x PL CO_2 cases (Figure 3.4a-d). The planet is entirely ice-covered, similar to the coverage illustrated in Figure 3.1a. The potential density structure in Ri10 experiences a similar spatial pattern to F10 (lighter water at the tropics and denser water at the poles; Figure 3.4b). The main difference is where the transition to denser water occurs. This gradient shifts poleward to ∼50°N/S and shoals to ∼600 m, from ∼40°N/S at ∼950 m in F10 (Figure 3.4a,b,e,f). Ri10 has lighter densities in the mid-latitudinal bands but slightly denser water in the tropical and polar regions compared to F10. The addition of the ridge leads to a poleward expansion and shoaling of lighter densities compared to F10. The density structure is similar to the temperature and salinity structures found in Wu et al. (2021). The same pattern is not apparent in Ro10, although there is a slight poleward expansion of lighter waters (Figure 3.4c,g) and an increase in density near the surface in the tropics. The differences in Ro10 density structure relative to F10 are often much smaller than the differences between Ri10 and F10, suggesting that the smaller, discontinuous bathymetric features are not sufficient to support the same ocean circulation and property changes as in Ri10. The RR10 simulation further demonstrates this. Despite the addition of rough bathymetry to the ridge case, the changes to the density structure are nearly identical to Ri10 (Figure 3.4d,h).

The MOC of all four simulations follows the same general pattern, with one overturning cell per hemisphere, upwelling at the equator, and downwelling at higher latitudes (Figure 3.5e-h). Within Ro10 (Figure 3.5g), the overturning cells extend poleward to 70°N/S compared to F10, in which they only reach 50°N/S (Figure 3.5e). There are three maxima within each cell; however, the two peaks confined within 50°N/S are stronger (∼5 Sv) than the maxima at higher latitudes (∼2 Sv). These extrema are attributed to the presence of varied seafloor features in Ro10, which either enhance or inhibit zonal and meridional flow depending on their location and orientation. For Ri10 and RR10, the MOC extends to 75°N/S (Figure 3.5f,h). Within the general MOC pattern, there are two maximum regions in the upper ocean, forming a 'bunny ear' structure, and a strong cell at depths below 700 m. The 'bunny ear' structures occur in the same locations as in F10. The depth below which the MOC strengthens coincides with the top of the ridge (depths greater than 650 m) (Figure 3.5f,h). This occurs because the ridge helps aid in the development of a deep western boundary current (DWBC)-like pattern along the ridge. The meridional currents within the DWBC-like structure reach speeds up to 8.7 cm s^{-1}. The integrated effect of the stronger boundary current is a stronger MOC. Ri10 (RR10) has a maximum strength of 6 Sv compared to the maximum strength of ∼4.5 Sv in F10.

The OHT within all four simulations also follows a similar structure, but with different spatial variations. Both hemispheres experience a poleward OHT, with a peak at 25°N (Figure 3.5a-d). OHT in F10 and Ro10 peaks at ∼1 PW, and Ri10 and RR10 peaks at ∼0.5 PW. The decrease in OHT within the ridge cases is attributed to the densities being lighter at lower latitudes, as the overall ocean in all four simulations is very cold. The meridional temperature gradient reduces in the ridge cases to -2.1 to -1.7°C, whereas F10 and Ro10's meridional temperature gradient is -2.1 to -1.6°C. Overall, the changes in OHT due to the presence of bathymetry are small, but bathymetry does alter the ocean's properties and circulation. These changes alone are not sufficient to significantly alter the global climate, which is more strongly dependent on the insolation and atmospheric CO_2 concentration.

3.2.2 500x CO_2

In the previous analyses, we saw that F10 and Ro10 behave nearly identically in terms of their OHT and MOC. A similar result holds for the Ri10 and RR10 simulations. Therefore, in the analysis of the higher atmospheric CO_2 simulations, only the Flat (F500) and Ridge + Rough (RR500) bathymetric configurations are considered.

F500 and RR500 experience the same sea ice coverage as well as a similar density structure, but with different magnitudes. In these simulations, the planet is ice-free (similar to Figure 3.1b). As discussed in Section 3.1, the zonal mean potential density structure of F500 is characterized by higher density water in the equatorial region and lighter density water at the poles (Figure 3.6a), which is a reversal from what occurs on modern Earth. RR500 has a comparable zonal mean density structure but a slightly shifted density range (Figure 3.6b). The density range for F500 is 20 to 30 kg m^{-3}, while in RR500 it is 23 to 34 kg m^{-3}. Both simulations experience a maximum in density at ∼25°N, associated with a region of very high atmospheric evaporation. With the addition of bathymetry, the ocean becomes saltier and colder, bringing about the increase in density (Figure 3.6c-f). The salinity increased from an average of 40.56 psu in F500 to an average of 48.31 psu in RR500, and the potential temperature decreased from an average of 31.21°C in F500 to an average of 29.89°C in RR500. The difference in salinities is linked to the amount of water in the ocean, as mentioned when comparing F10 and F500. In F500, the SSH (not shown) suggests ∼240 m of water is lost, and in RR500, ∼388 m of water is lost, leading to the large salinity increase in RR500 (salt stayed in the ocean, while water was removed). Additionally, there is an asymmetric response across the ocean, which is further explored in Chapter 4.

The MOC of F500 and RR500 behave similarly. In F500, one strong cell, circulating clockwise, sits on the equator spanning 25°N/S, and a weaker cell, circulating counter-clockwise, occurs off the equator, confined to 25 to 45°N (Figure 3.7c,d). Associated with this circulation pattern is downwelling at 25°N and upwelling at 25°S. RR500 follows the same pattern, but with some small differences. In the clockwise cell, the largest values of the overturning extend to deeper depths (700 m in F500 versus ∼950 m in RR500). The strengthening at depth is a result of strong meridional currents, creating a DWBC-like structure as in R10. In addition, the counterclockwise cell weakens by ∼15 Sv and shoals, reaching a depth of only 700 m versus the seafloor (1,360m) in F500. This occurs because the meridional currents are very strong within the bathymetric simulation (peaking at 8.6 cm s^{-1}).

The OHT structure in RR500 is similar to F500 (northward from 90°S to 25°N, and southward from 25 to 90°N), but the overall magnitude increases, as the maximum more than doubles. F500 peaks at ∼6 PW and RR500 peaks at ∼14.5 PW, both at 10°N (Figure 3.7a,b). Both experience a higher OHT than modern Earth, which is attributed to the ocean being in a much warmer overall state. Both simulations have a temperature range of 5 to 40°C, where F500 has an average potential temperature of 31.21°C, while RR500 has an average potential temperature of 29.89°C. The increase in OHT in RR500 relative to F500 is due to the increase in density throughout the entire ocean (F500's range is 20 to 30 kg m^{-3}, RR500's range is 23 to 34 kg m^{-3}), and the increase in meridional current speeds (e.g., at 1,130 m, F500's meridional velocities peak at 0.12 cm s^{-1}, and RR500's peak at 5.1 cm s^{-1}), as density and meridional currents are accounted for in the OHT calculation. Figure 3.8 highlights the different meridional current structures at various depths in the ocean.

3.2.3 Atmospheric CO_2 Comparison

Across all the 10x and 500x atmospheric CO_2 concentration simulations, there are differences in the ocean properties and circulation when bathymetry is added to the seafloor. In addition, the low CO_2 concentration yields an ice-covered planet, while the high CO_2 concentration yields an ice-free planet. The zonal mean potential density, MOC, and OHT all change due to the addition of bathymetry, but the specific changes that occur are not always the same under different CO_2 concentrations. For the zonal mean potential density, the spatial pattern changes within the 10x bathymetry cases with little change in the density range, but both the spatial pattern and density range change drastically between the 500x cases. The MOC in the 10x cases increases in strength with the addition of bathymetry, but the changes in the structure depend on what bathymetric features are present. There are slight variations in the MOC structure in the 500x cases due to the presence of bathymetry, and both F500 and RR500 have similar MOC magnitudes. For the OHT, the spatial pattern experiences no large change in the 10x cases, but the magnitude halves when a ridge is present within the simulation. Unlike in the 500x cases, the spatial pattern of the OHT in each simulation is similar, but the magnitude more than doubles in the presence of bathymetry. Overall, bathymetry alters the ocean state, with stronger impacts on the density ranges, MOC, and OHT at the high CO_2 concentration. These results suggest that bathymetry may impact ocean circulation and properties differently depending on the ocean's mean state and other environmental parameters.

3.3 Influence of Salinity

Up to now, the salinity in all the simulations has been initialized with modern Earth salinity (35 psu). This section contains the analysis of the influence of salinity by increasing the initial salinity to a high salinity (50 psu) at both the high and low CO_2 levels. These simulations are done with a flat-bottom ocean to solely investigate the impact of salinity on the ocean properties and circulation. We look at the spatial pattern of sea ice coverage and density, and the spatial pattern and magnitude of the MOC and OHT.

The two average salinities, modern and high salinity, yield sea ice coverage changes in the low CO_2 concentration cases. Increasing salinity from 35 psu to 50 psu in the Flat 10x cases leads to a reduction in sea ice cover and the formation of a slushy belt–an area with a mix of ice and water–within the equatorial region (Figure 3.9b). Other studies note a similar feature, although the "slushy belt" in these cases is often an ice-free water belt, and attribute the stabilization of the belt to sea ice albedo feedbacks and strong wind-driven ocean overturning at low latitudes (Abbot et al., 2011, Olson et al., 2022, Rose, 2015). In F500-50, no slushy belt exists because the planet remains ice-free like its F500 counterpart (Figure 3.9c,d).

The zonal mean potential density structures within F500 and F500-50 are similar to each other (Figure 3.10). Moreover, the density values are on average ∼3 kg m^{-3} higher throughout the entire ocean in F500-50 (Figure 3.10b). This increase in density is attributed to the increase in salinity (an increase of ∼6 psu globally), as the ocean's potential temperature experiences very little change relative to F500. Like F500, however, F500-50 exhibits a maximum in density at the surface at ∼25°N, indicating a region of strong downwelling and dense water formation. As a result, the overall structure of the MOC is similar in both simulations at 25°S (Figure 3.12g,h). The OHT patterns in F500 and F500-50 are also similar. Both experience a northward OHT from 90°S to 25°N, and switch to southward OHT from 25 to 90°N (Figure F3.12c,d). The only difference is the maximum value: F500 peaks at ∼6 PW at 25°N, while F500-50 peaks at ∼7.5 PW at 25°N. The increase in OHT in F500-50 is likely due to the shift to higher densities in this simulation, as the meridional current velocities and temperature are similar to F500.

While the F500 and F500-50 are similar, the F10 and F10-50 vary from each other. F10 has a bowl-like structure of low density in the tropics and denser water at the poles, but a similar structure does not form in F10-50 (Figure 3.11). In the ice-free region of F10-50, an area of very low density water forms in the upper 200 m in the equatorial region, and below this, the water is much denser. The water also increases in density at the sea ice edge (∼20°N/S), due to brine rejection from sea ice formation (Figure 3.11b). Outside of the equatorial region, hemispheric asymmetries are present in the ocean, similar to results in Section 3.2.2; these will be discussed in Chapter 4.

The MOC and OHT also change between F10 and F10-50. F10's MOC experiences one cell per hemisphere, with a peak of ∼4.5 Sv (Figure 3.5e), but the slushy belt in F10-50 leads to changes to the MOC structure. There is one strong cell per hemisphere consisting of an upwelling arm along the equator and a downwelling arm at the ice edge at ∼20°N/S (Figure 3.12f). In the slushy regions, the MOC strengthens to ∼40 Sv, attributed primarily to the brine rejection at the sea ice edge. Beyond the sea ice edge, the MOC is < 10 Sv, resembling F10 in the same regions. The OHT of both simulations is poleward. F10 peaks at ∼1 PW at 25°N, and F10-50 peaks at ∼3 PW at 10°N (Figure 3.12a,b). Despite F10-50's ocean being ∼1.5°C colder on average, the increased salinity leads to an increase in density, resulting in an overall increase in the OHT.

Overall, salinity has a strong impact on ocean properties and circulation. These impacts are larger in the 10x CO_2 concentration simulations compared to the 500x CO_2 simulations due to the impact salinity has on sea ice. In the slushy belt in F10-50, strong downwelling due to brine rejection at the sea ice edge leads to the development of a strong overturning cell on either side of the equator. The influence of salinity at the high CO_2 concentration is reflected primarily through the increase in density in F500-50 rather than in the ocean's circulation. As a result, the MOCs are similar between the two simulations, and the OHT increases in F500-50 solely due to the increase in density from the increased ocean mean salinity. These results suggest salinity can have a larger role in ocean circulation when there is sea ice present on the planet.

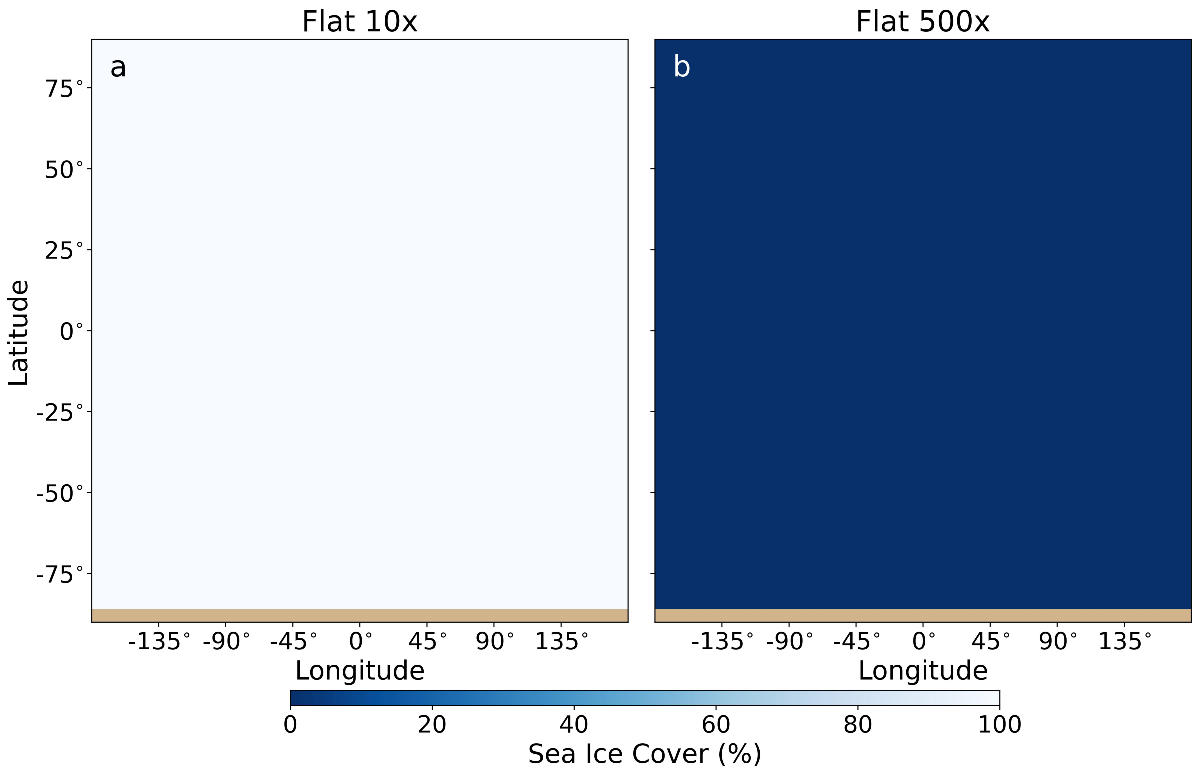

FIGURE 3.1: Global sea ice coverage (%) for (a) F10 and (b) F500 simulations. The brown strip at the South Pole is land. The land is present throughout all simulations.

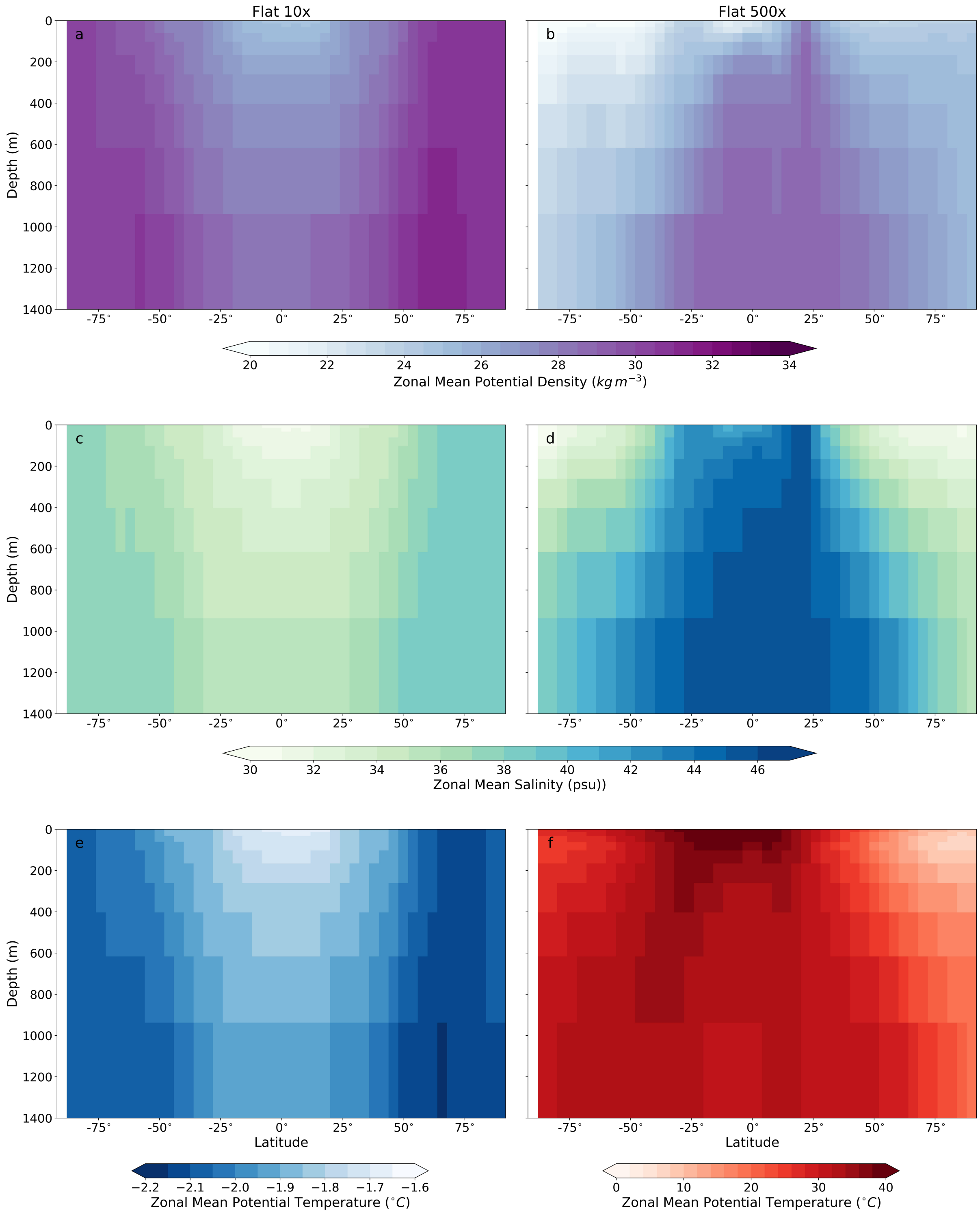

FIGURE 3.2: Zonal mean (a,b) potential density (kg m^{-3}), (c,d) salinity (psu), and (e,f) potential temperature (°C) in F10 (a,c,e) and F500 (b,d,f). The zonal mean potential temperatures are on different scales to capture the different ocean states.

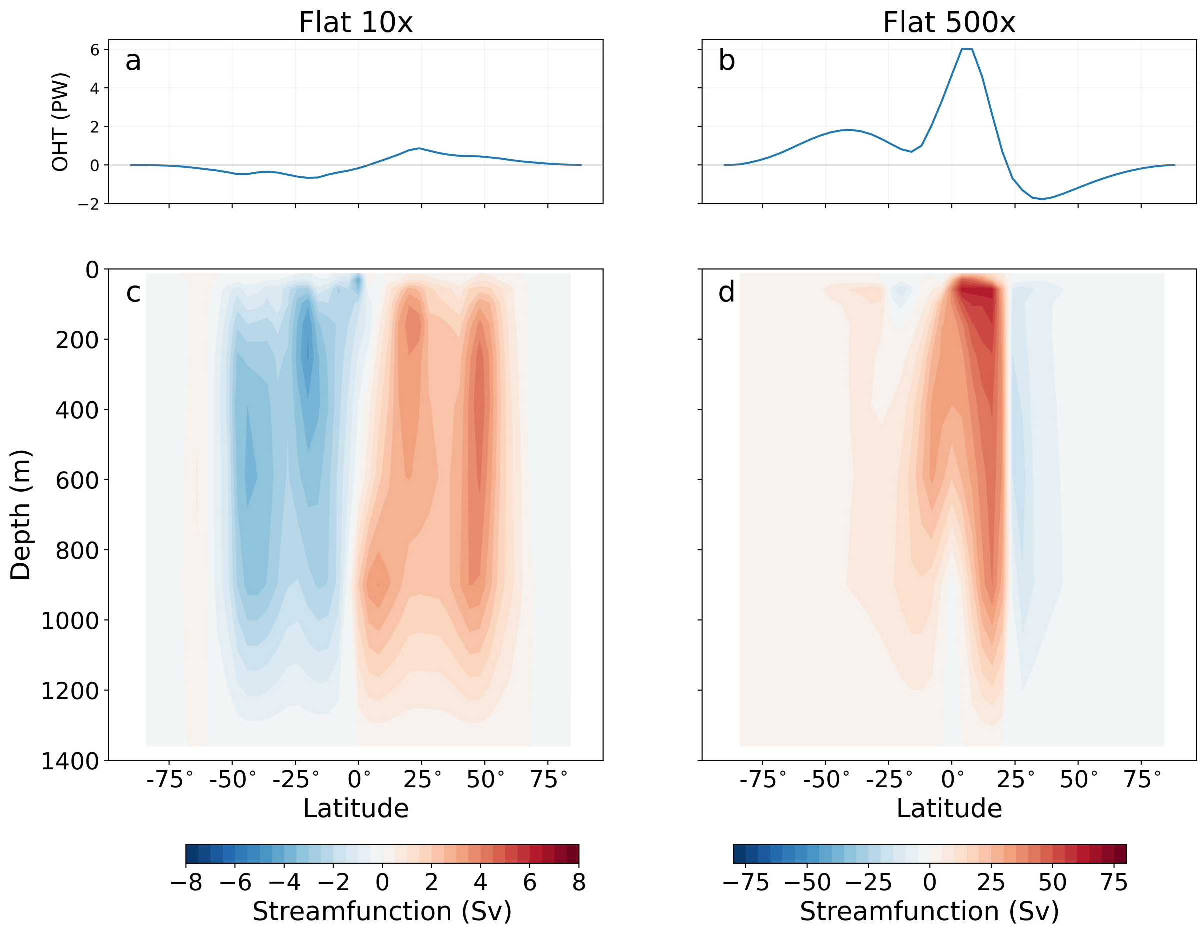

Figure 3.3: Meridional (a,b) oceanic heat transport (PW), and (c,d) oceanic streamfunction (Sv) in F10 (a,c) and F500 (b,d). The meridional oceanic streamfunction shows the MOC. The meridional streamfunctions are on different scales to capture the different ocean states, as F500 is an order of magnitude larger.

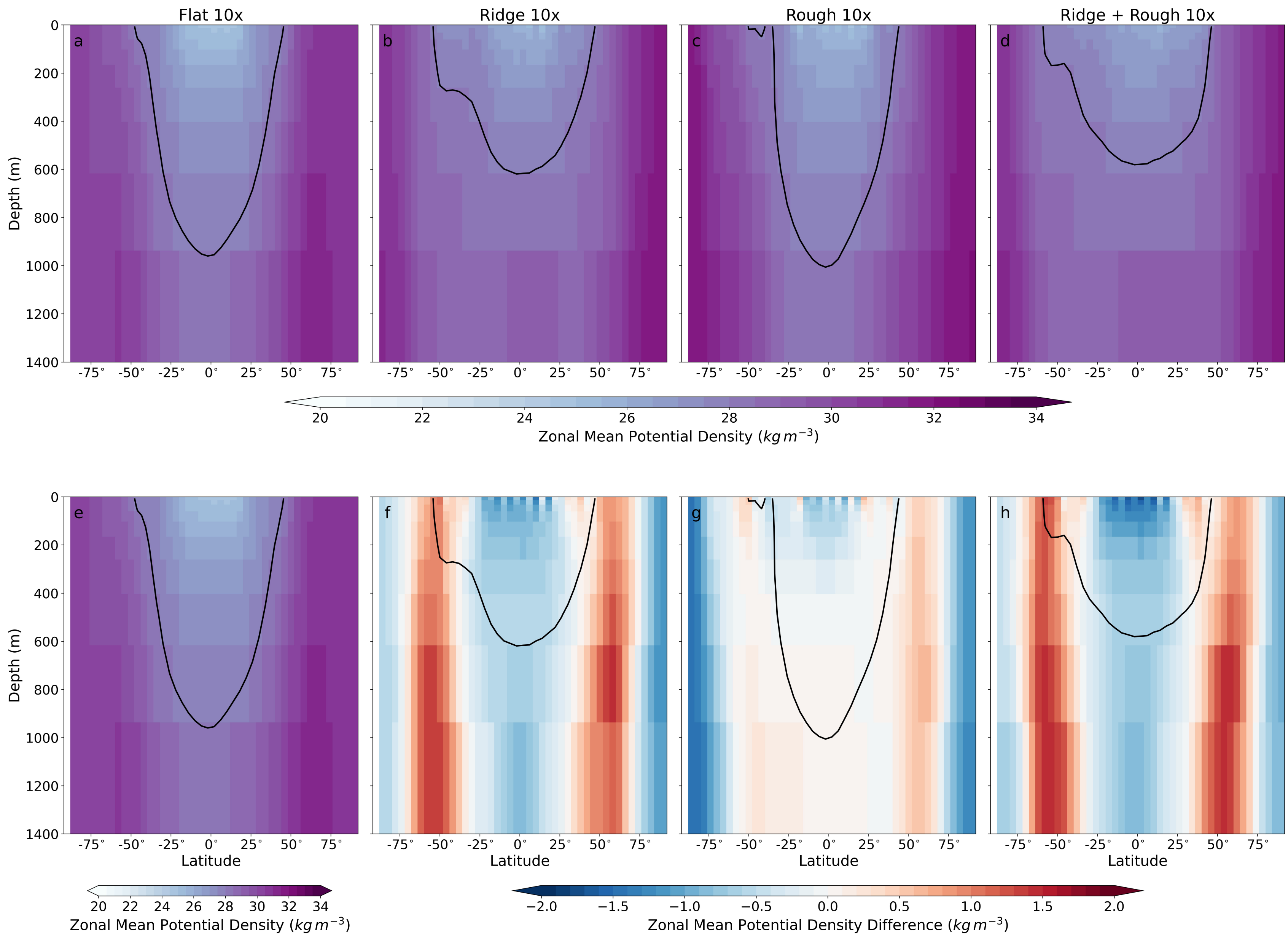

FIGURE 3.4: Zonal mean (a-e) potential density (kg m^{-3}), and (f-h) difference in the density structures in each bathymetry case (Flat - Bathymetry) in F10 (a,e), Ri10 (b,f), Ro10 (c,g), and RR10 (d,h). Reds (blues) represent higher (lower) density in the control simulation, F10. The black line is each simulation's 28 kg m^{-3} density contour.

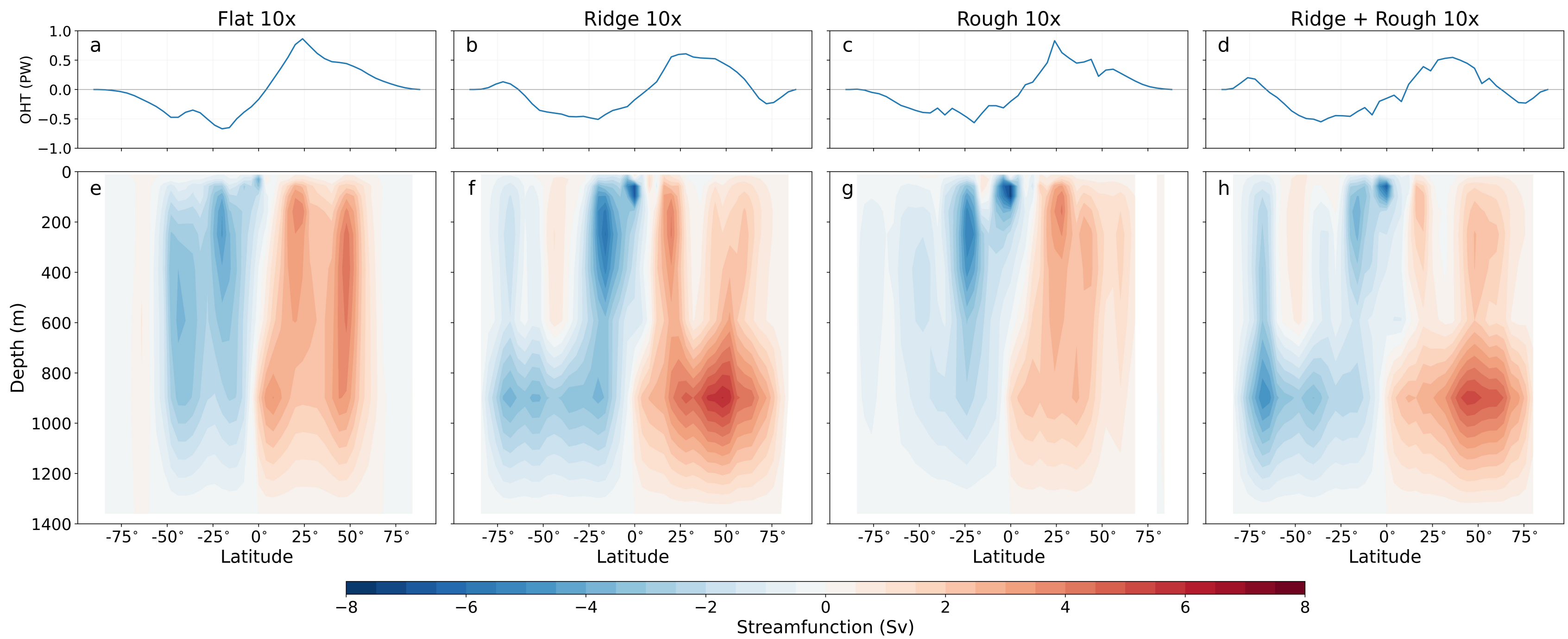

FIGURE 3.5: Meridional (a-d) oceanic heat transport (PW), and (e-h) oceanic streamfunction (Sv) in F10 (a,e), Ri10 (b,f), Ro10 (c,g), and RR10 (d,h).

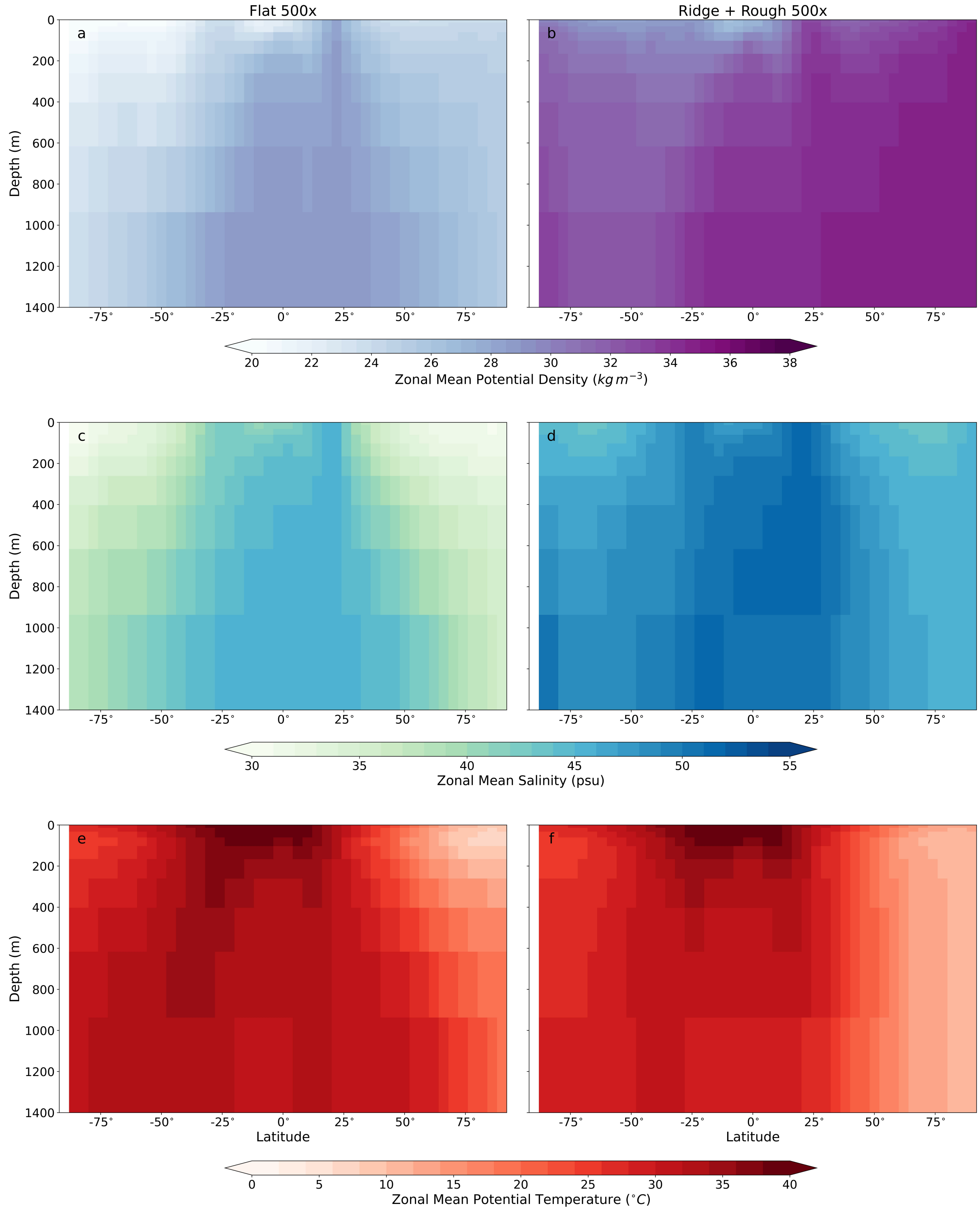

FIGURE 3.6: Zonal mean (a,b) potential density (kg m^{-3}), (c,d) salinity (psu), and (e,f) potential temperature (°C) in F500 (a,c,e) and RR500 (b,d,f).

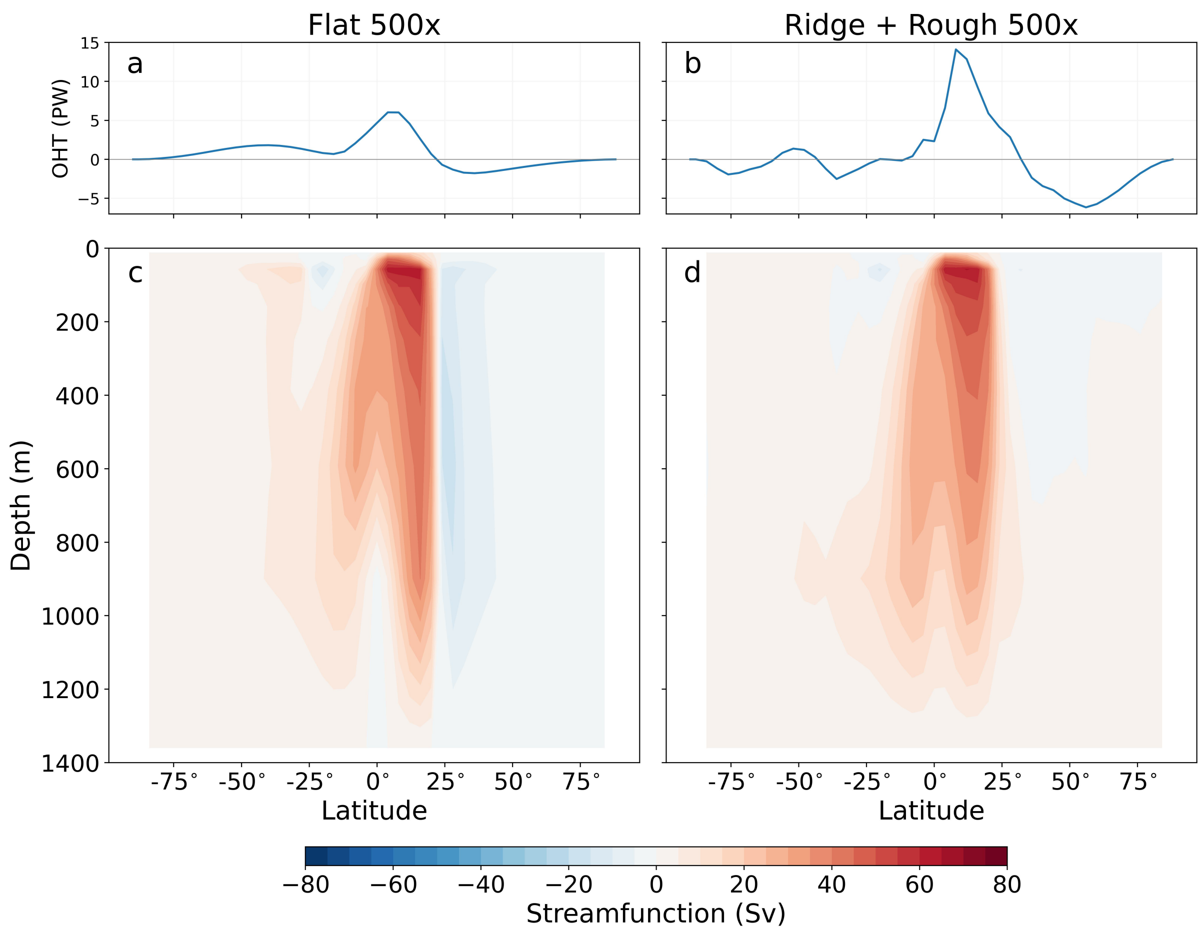

FIGURE 3.7: Meridional (a,b) oceanic heat transport (PW), and (c,d) oceanic streamfunction (Sv) in F500 (a,c) and RR500 (b,d).

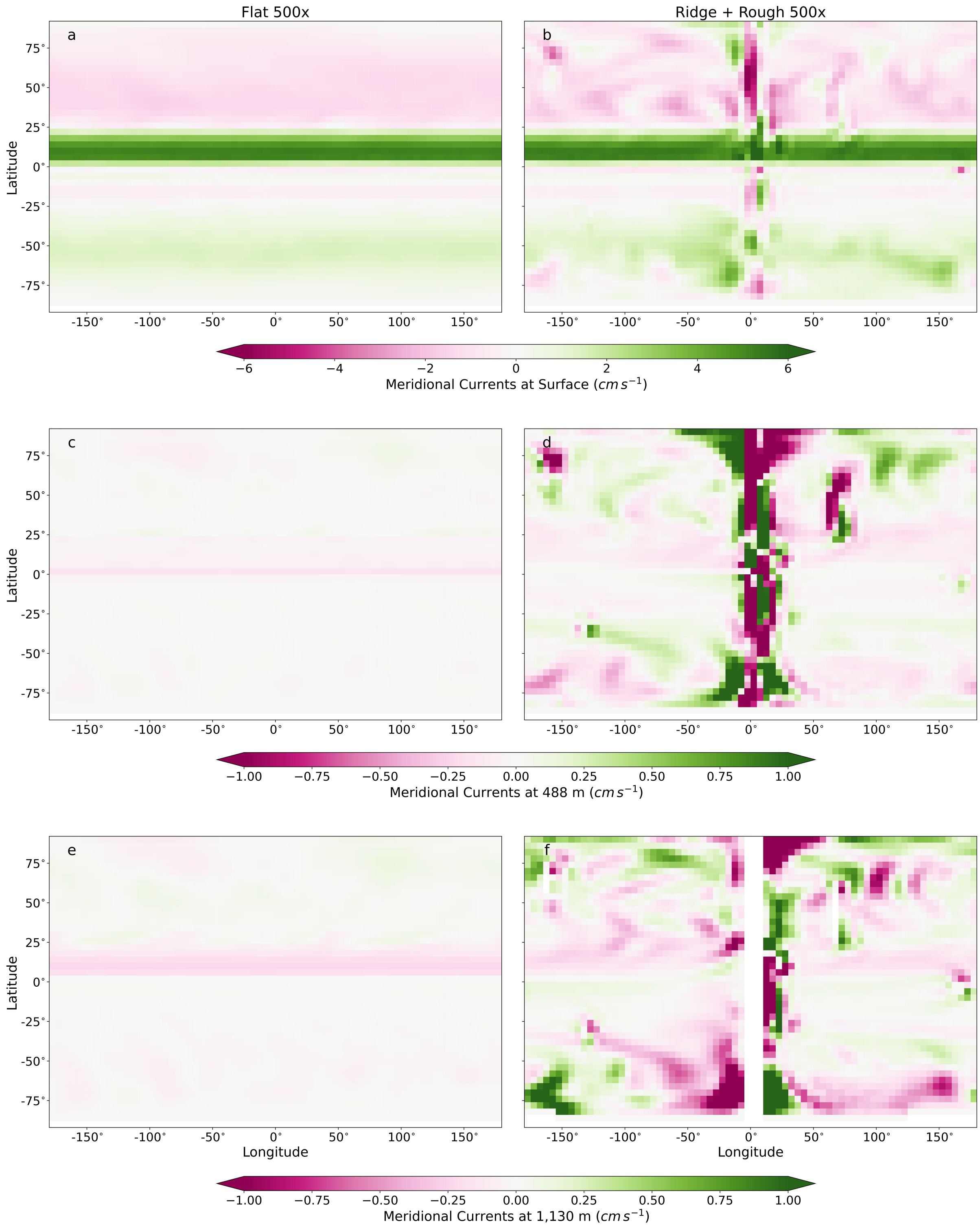

FIGURE 3.8: Ocean meridional currents (cm s^{-1}) at (a,b) the surface, (c,d) 488 m, and (e,f) 1,130 m in F500 (a,c,e) and RR500 (b,d,f). The scale for 488 m and 1,130 m is different from that of the surface currents to best capture the meridional current structures.

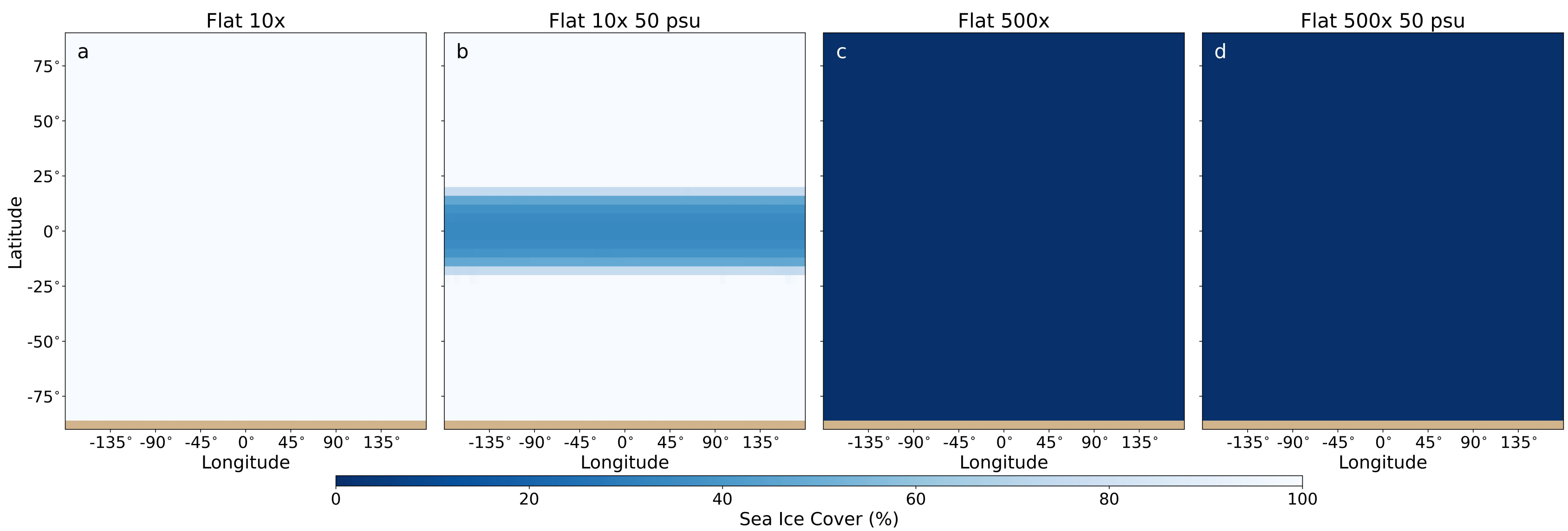

FIGURE 3.9: Global sea ice coverage (%) for (a) F10, (b) F10-50, (c) F500, and (d) F500-50 simulations. The brown strip at the South Pole is land.

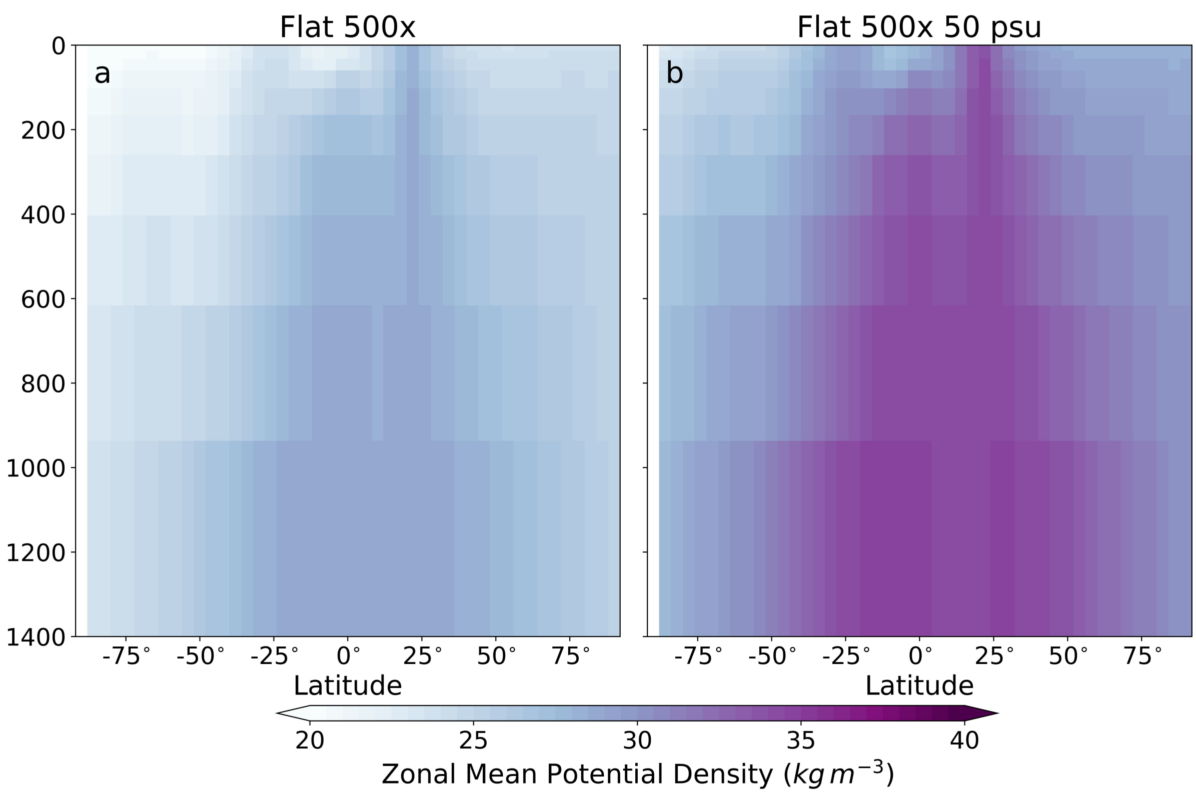

FIGURE 3.10: Zonal mean potential density (kg m^{-3}) in F500 (a) and F500-50 (b).

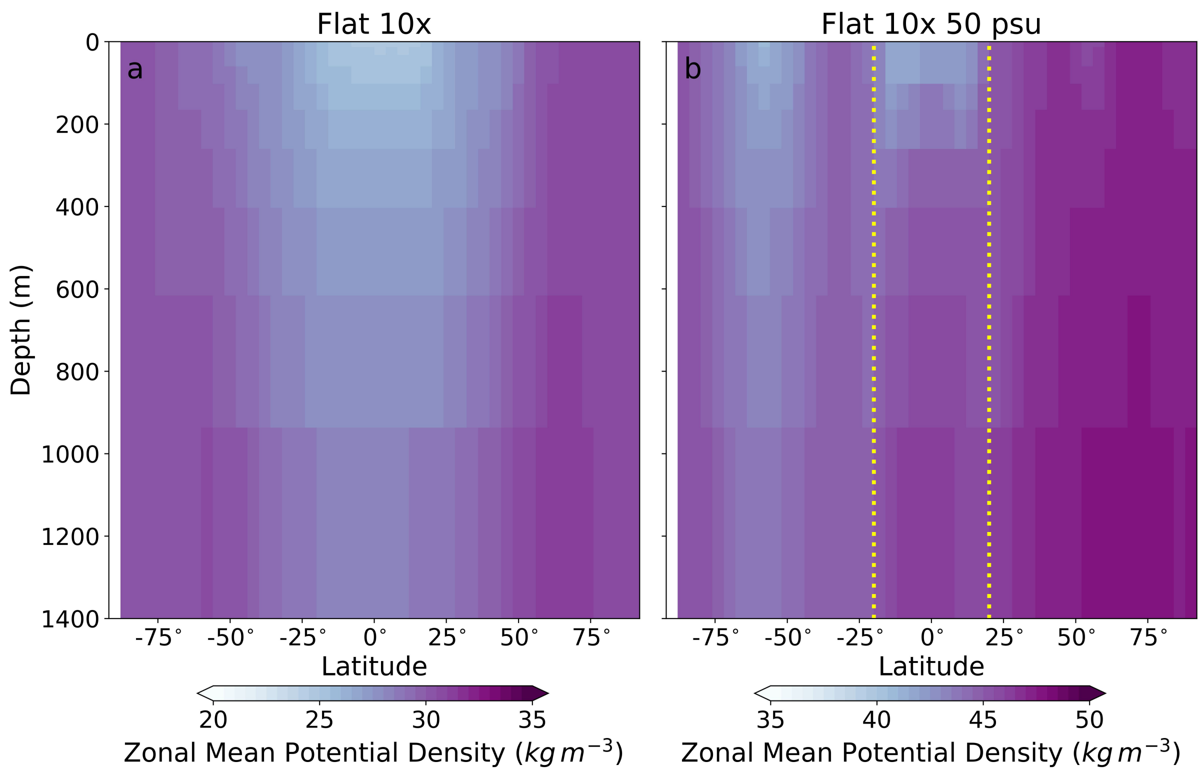

FIGURE 3.11: Zonal mean potential density (kg m^{-3}) in F10 (a) and F10-50 (b). The yellow contour indicates the sea ice edge in F10-50. The scale of F10-50 starts where F10 ends at 35 kg m^{-3} due to the difference in ocean states.

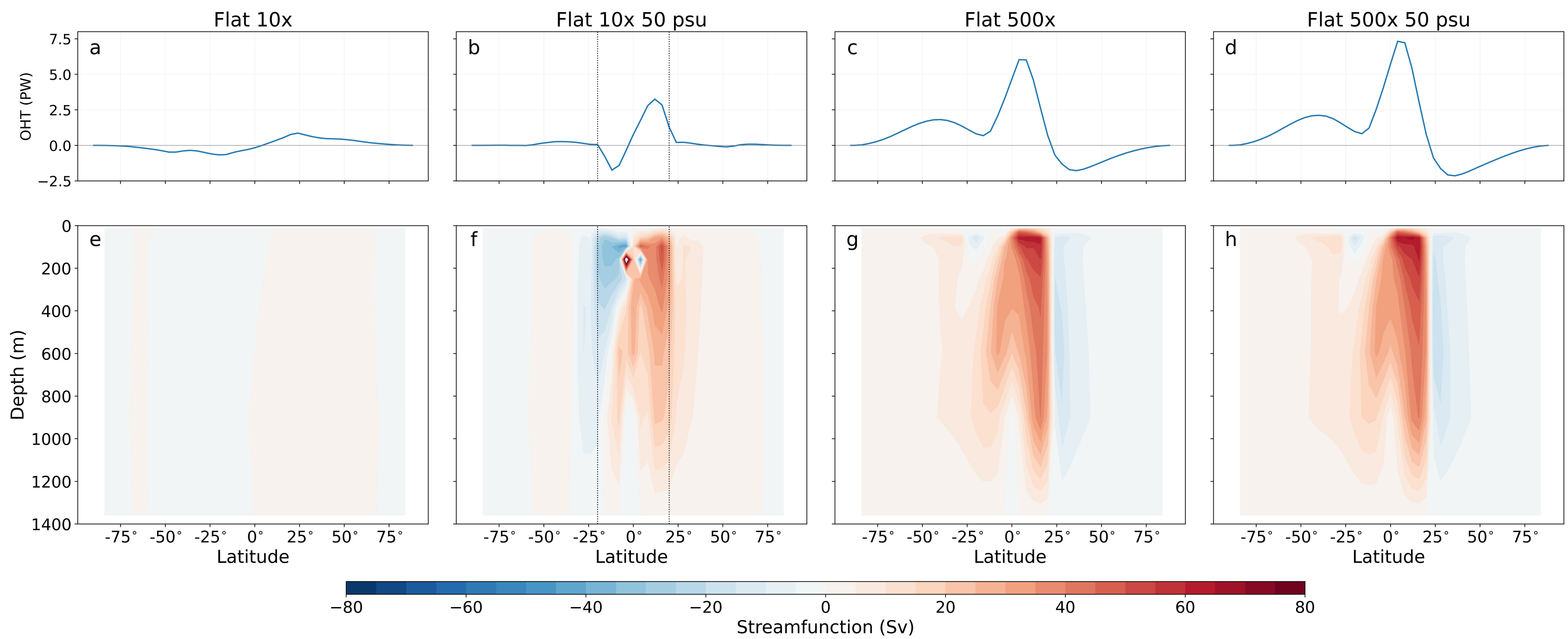

FIGURE 3.12: Meridional (a-d) oceanic heat transport (PW), and (e-h) oceanic streamfunction (Sv) in F10 (a,e), Fi10-50 (b,f), F500 (c,g), and F500-50 (d,h). The dashed contour indicates the sea ice edge in F10-50. For a detailed look at the streamfunction of F10, look at Figure 3.5e.

Chapter 4

Discussion and Conclusion

4.1 Discussion

The goal of this research has been to better understand the possible ocean circulation and ocean states within the early Archean Eon, when the first ocean developed on Earth. Because of this, the analysis focused mostly on ocean properties and dynamics and contained limited discussion of the atmospheric component of the Archean climate system. The parameters explored within this thesis, via sensitivity tests, were atmospheric CO_2, ocean bathymetry, and salinity. The findings from each of these are summarized and discussed below.

4.1.1 Atmospheric CO_2

The results show that the CO_2 concentration has a large impact on the ocean's mean state. Moreover, in this thesis, the two CO_2 concentrations simulated have opposite or reversals in their mean states when comparing them. In the low CO_2 simulations, the planet experiences complete ice coverage, with homogeneous cold ocean temperatures, but in high CO_2 simulations, the planet is ice-free, and ocean temperatures are much warmer, spanning a large range. At both CO_2 levels, the density forms a bowl-like structure, where the low (high) concentration has lower (higher) densities at low latitudes and higher (lower) densities at high latitudes (Figure 3.2a,b). There are large differences in the structure and magnitudes of both MOC and OHT as well (see Figure 3.3).

The two CO_2 levels tested in this thesis fall within the large estimation range CO_2 of the Archean Eon from proxies, showing the importance of capturing the extreme ends of what could have occurred to best represent the possible Archean ocean and climate, as both CO_2 concentrations yielded difference ocean states. The results presented by these two simulations agree with previous work done with aquaplanets and paleoclimate studies. Past glaciated environments, such as a snowball Earth or the Pleistocene Epoch (2.58 million years ago to 11,700 years ago), experienced a weaker MOC and OHT (i.e., Brunetti et al., 2019, Kim et al., 2021). However, warm climates, such as an ice-free planet or the Eocene Epoch (56 to 33.9 million years ago), experience a stronger MOC and OHT (i.e., Brunetti et al., 2019, Zhang et al., 2020, 2022). From the mentioned studies, the ocean states achieved in this thesis are plausible for the Archean on both ends of the CO_2 proxy range.

4.1.2 Bathymetry

Overall, F10 and Ro10 exhibit very similar density patterns, circulations, and heat transports, and the same is true for Ri10 and RR10. Due to these similarities, the primary focus is on F10 and RR10 in the discussion below.

At the low CO_2, all four simulations broadly resemble modern Earth's structures for density, with lighter density water at low latitudes, higher density water at high latitudes, as well as the OHT, with a net poleward transport (Figure 3.5a-d). However, the OHT magnitudes are reduced due to the absence of any landmass; furthermore, the ridge cases experience weaker OHT attributed to a large region of lower density water at low latitudes (Figure 3.4). In all four simulations, the MOC's magnitude is < 6 Sv, which is less than half of what modern Earth observations show. Each is characterized by one large cell per hemisphere, but RR10 has an additional localized maximum at depth (attributed to the DWCB-like structure along the ridge) (Figure 3.5e-h). Despite changes in the large-scale circulation due to the addition of bathymetry, the planet remains ice-covered due to the low insolation.

All four bathymetric configurations tested yield different ocean states, however, the strength of these changes depends on the bathymetric features and their size. The largest changes are between the Flat and Ridge + Rough simulations, as discussed throughout this thesis. The smallest changes are between Flat and Rough, and Ridge and Ridge + Rough. This showcases how the smaller bathymetric features in the Rough configuration can alter the ocean, but their smaller, discontinuous bathymetric features are not sufficient to support the large changes in the ocean state experienced in ridge cases. Indicating, the size alone of bathymetric features can have an impact on the ocean properties and dynamics.

At the high CO_2 concentration, the warming from the increased CO_2 concentration is large enough to overcome the cooling from the low insolation, resulting in an ice-free planet. In both F500 and RR500, the density's spatial structures are similar, however, RR500 is globally more dense than its flat counterpart, attributed to an increase in average salinity. In RR500, the MOC's clockwise cell broadens at low latitudes and the counterclockwise cell weakens poleward of 25°N (Figure 3.7c,d). Additionally, the OHT structure is similar across both simulations, but F500 peaks at ~6 PW and RR500 peaks at ~14.5 PW (Figure 3.7a,b). Both the changes in MOC and OHT are attributed to the development of a DWBC-like structure along the ridge. Furthermore, the OHT increase in RR5000 is influenced by the increase in density throughout the entire ocean.

In these high CO_2 simulations, there is an asymmetric response in the ocean's potential density, as mentioned in Section 3.2.2, and can be seen in Figure 3.6a,b. The Northern Hemisphere high latitudes are overall denser than the Southern Hemisphere, giving rise to the asymmetry across the planet. Compared to Wu et al. (2021), our results align with the decrease in temperature when there is bathymetry, but they do not agree for salinity: our results show a large change, while Wu et al. (2021) does not. Moreover, their study shows that the planet experiences an equatorially symmetric change in ocean circulation and properties, whereas we do not, despite running with a similar obliquity (Wu et al. (2021) used 23.3°, while we used 23.5°); there is no discussion on other orbital parameters in Wu et al. (2021). The asymmetry can also be seen in the SSH (not shown), but more analysis is required to understand these responses, as well as the differences between previous literature and the presented work.

At both CO_2 concentration levels, the addition of bathymetry alters the ocean properties and circulation, but these alterations depend on the environmental configuration. For example, the density overall lightens in the 10x cases in the presence of a ridge, but the 500x case increases in density. Additionally, the OHT in the 10x cases decreases by half in the presence of a ridge, but the 500x case doubles. More analysis is required to understand why these responses are opposites. Nevertheless, these results illustrate how the ocean's response to the addition of bathymetry does not cause the same shift within the two CO_2 regimes simulated. They also suggest that bathymetry does not have a strong impact on the overall pattern of meridional ocean heat transport, both generally and as compared to other parameters such as atmospheric CO_2 concentration or ocean salinity.

4.1.3 Salinity

In the low CO_2 simulations, F10-50 develops a slushy belt in the equatorial region due to warmer water in the tropics and stabilizes via strong ocean overturning from wind and brine rejection, while F10 experiences global sea ice coverage (Figure 3.9a,b). The sea ice coverage has large impacts on the MOC, OHT, and density structure. In the slushy belt region in F10-50, the MOC and OHT are very strong compared to the fully ice-covered ocean in F10 (3.12a,b,e,f). Poleward of 20°N/S (where the sea ice edge sits in F10-50), the MOC and OHT look similar, due to both planets being ice-covered. The changes in MOC and OHT are attributed to the brine rejection at the sea ice edge, which results in dense water formation. The density structure and ranges are starkly different between F10 and F10-50, and there is hemispheric asymmetry in F10-50. One plausible explanation is the influence of obliquity. In the presented work, an obliquity of 23.5° is used. However, in a short simulation with an obliquity of 0°, which has yet to achieve steady-state and is not shown, it has a hemispherically symmetrical MOC. These results require an in-depth analysis to understand the physical differences between the simulations and the response to obliquity, as well as how ROCKE-3D parameterizes the planetary parameters.

In the high CO_2 simulations, there are no differences in sea ice because the planet is ice-free. The density structures in both salinity cases are similar, but F500-50 is globally denser by $\sim$3 kg m^{-3} due to the increase in salinity (Figure 3.11). The structure and magnitude of the MOC are the same across both simulations (Figure 3.12g,h). The OHT of F500 peaks at $\sim$6 PW at 25°N, while F500-50 peaks at $\sim$7.5 PW at 25°N (Figure 3.12c,d). The increase in OHT magnitude is attributed to the overall increase in density within F500-50.

Overall, the results of the salinity simulations suggest that the relative importance of salinity in setting ocean circulation patterns may change in cold, ice-present versus warm, ice-free climates. Changing the salinity in the low CO_2 concentration simulations leads to large differences in the ocean properties and circulation, while changes in salinity in the high CO_2 concentration simulations lead to little change in the ocean properties and circulation beyond an overall increase in density. This suggests salinity has a larger role in controlling the ocean dynamics in the low CO_2 cases because it influences the sea ice coverage, and it also suggests that salinity could potentially counteract the influence of the CO_2 concentration on a planet, at least in terms of ice coverage, in agreement with the findings of Olson et al. (2022). Moreover, both CO_2 cases highlight the importance of sea ice cover (including its absence) on ocean dynamics, a result that is supported by previous findings (i.e., Brunetti et al., 2019, Enderton and Marshall, 2009, Ferreira et al., 2011, Muilwijk et al., 2024, Rippeth and Fine, 2022).

4.2 Caveats and Limitations

As expected, errors and other uncertainties come along with this work. Most of the uncertainties originate from how ROCKE-3D is designed. The resolution of ROCKE-3D is 4° latitude x 5° longitude (Way et al., 2017). This coarse resolution is a positive because it allows for parameter space explorations at a low computational expense, but it strongly limits what the model can resolve, including dynamical processes, bathymetric features, and/or the interaction between the two. Most meso- and micro-scale features are not captured at all by the model beyond basic parameterizations such as those for eddies. Many studies have shown that model resolution has a large impact on ocean circulation and heat transport on modern Earth (i.e., Covey, 1995, Grist et al., 2018, Roberts et al., 2020). With Earth's faster rotation rate in the Archean, the role of eddies in ocean heat transport and circulation could be more important, but their total impact is likely not captured by this model, nor are small-scale interactions with complex topography. The sea ice component of the model is also problematic, often leading to the sea ice becoming unrealistically thick, potentially inhibiting air-sea exchange that might otherwise be present, or at least more impactful than the results suggest. It also required us to run the model at very high CO_2 levels (500x PL) to completely remove the sea ice. Lastly, as seen in F10, F500, and RR500, there is a large loss of water from the ocean that is not being accounted for in the other components of the model. Where the water goes and how the model parameterizes this water loss needs to be further investigated. Despite these model issues, ROCKE-3D is still a useful tool for understanding the "big picture" aspects of a planet's climate. However, it may be less appropriate for more detailed oceanographic studies that push the limits of the model, as have been done here.

The limited data available to understand the Archean Earth also needs to be considered. Due to how long ago the Archean was, very little geologic evidence of this period exists; most of the rock from this time has been reintroduced or recycled back into the complex systems occurring on Earth. With such limited geological records, we chose parameters that could bracket their possible ranges, hence the sensitivity testing. The sensitivity tests are included in this project to help see the full spectrum of what the ocean, climate, and Earth could have looked like billions of years ago, but testing all of the possibilities isn't feasible with this model, and even less so with one of higher resolution. For example, here was potentially an organic haze present throughout the Archean Eon due to the large abundance of methane within the atmosphere (Arney et al., 2016). The results could be different than what is shown if there was a haze present, as the haze would act to cool the planet. The chemistry required for this is currently too complex for the framework of ROCKE-3D, although there is work being done to add haze and other aerosols to the model.

4.3 Conclusion

While there are several caveats and limitations within this study, we were able to investigate the influence of atmospheric CO_2, bathymetry, and salinity on early Archean ocean circulation in a suite of coupled GCM simulations. This work showed how increasing atmospheric CO_2 can alter the ocean via increased ocean temperatures and changes in density and circulation, how bathymetry alters the ocean via changes in circulation and ocean heat transport, and how salinity alters the ocean via changes in sea ice coverage, ocean circulation, and density.

The results from this thesis can be used to help further our understanding of the earliest ocean on Earth. We may also be able to use this information to start trying to understand where life developed on Earth by connecting the physical circulation to the prebiotic chemistry in the ocean at that time. Moreover, these lessons can be applied more broadly to the planetary science community. Exploring the ocean properties on an aquaplanet configured in an environment far removed from modern Earth is often the starting point for exoplanet studies, and at present, early Earth is the only testbed we have for understanding the origin of life.

Chapter 5

Future Work

On modern Earth, nutrient and chemical cycling are partially driven by ocean circulation. Upwelling regions supply nutrient-rich water to the surface while downwelling regions pump nutrient-depleted water to depth. The nutrients needed for life to develop can be assumed to have responded similarly to ocean physics. This means that changing the ocean circulation could change the connectivity between the surface and deep ocean, and thus nutrient cycling, through altering the locations of upwelling and downwelling. The work presented in this thesis shows that different atmospheric and oceanic conditions, including the presence of bathymetry, lead to changes in the overall differences in the ocean states via analysis of sea ice coverage, density structures, MOC, and OHT of the Archean Eon's ocean.

Our next steps are to further investigate the ocean circulation found in the presented work by looking at the role of the horizontal circulation and the role of wind-driven and buoyancy-driven circulations. The roles and partitioning of these circulations' influence on the ocean state on an aquaplanet may be altered from our knowledge of modern Earth's oceans. For example, the centers of wind-driven gyres on modern Earth experience downwelling, leading to a biologically dead region, or a region lacking an abundance of nutrients to support life. On the simulated Archean planet, in the high CO_2 cases, the surface currents are being forced by the wind, resulting in upwelling and downwelling occurring at the surface. However, in the low CO_2 cases, the wind-driven circulation is dampened due to sea ice, therefore, some other circulation, or ocean energetics, influences the vertical motion in the water column to move the nutrients. To understand where life development is plausible on the planet and in the water column, we need to determine the roles of the various influences on the overall ocean circulation.

We can also investigate the atmospheric component of the system, more specifically, the atmospheric heat transport and total heat transport. Doing so will allow us to perform a more in-depth analysis of the overall climate of the planet and help us understand the role of the atmosphere in driving the ocean under different conditions. Previous modern-day forced aquaplanet work shows how the partitioning of meridional heat transport is similar to modern Earth (e.g., Enderton and Marshall, 2009, Smith et al., 2006, Wu et al., 2021), but little has been done to determine if this occurs on an Archean Eon forced aquaplanet. On modern Earth, the partitioning of oceanic and atmospheric heat transports allows for our planet to be habitable. If this partition is different, we have to rethink the habitability of the planet, such as whether a region is more favorable to life than another on the globe.

Finally, as discussed in the caveats, ROCKE-3D is a good tool to use when answering exploratory questions about a planet's climate. However, for a more in-depth analysis, using a more complex coupled GCM is necessary. One example of a more complex model that can be used is the MITgcm, which has a horizontal resolution of 2.8° (Marshall et al., 1997a,b) but can be run at finer resolutions. Using the MITgcm can help to validate results from the ROCKE-3D simulation, but also the higher resolution can help to resolve more features within the ocean, impacting the ocean circulation and OHT. Moreover, if we wanted to simulate a more realistic Archean ocean, the MITgcm allows geothermal heating to be added to the simulations. Archean Earth had both deep ocean and shallow-sea hydrothermal vent systems (de Wit and Furnes, 2016). The origin of life is believed to have evolved in the extreme environments surrounding the hydrothermal systems (Lepot, 2020). This is attributed to the chemistry of the planet being controlled by the hydrothermal fluids and volcanic emissions of early Earth (Lepot, 2020). Therefore, the inclusion of the geothermal heating makes the Archean system more complex, but it also makes it more realistic to what is theorized to have existed.

Bibliography

Abbot, D. S., A. Voigt, and D. Koll, 2011: The Jormungand global climate state and implications for Neoproterozoic glaciations. *Journal of Geophysical Research: Atmospheres*, **116 (D18)**, doi:10.1029/2011JD015927, URL https://onlinelibrary.wiley.com/doi/abs/10.1029/2011JD015927, _eprint: https://onlinelibrary.wiley.com/doi/pdf/10.1029/2011JD015927.

Albarede, F., F. Thibon, J. Blichert-Toft, and H. Tsikos, 2020: Chemical archeoceanography. *Chemical Geology*, **548**, 119 625, doi:10.1016/j.chemgeo.2020.119625, URL https://www.sciencedirect.com/science/article/pii/S0009254120301649.

Arney, G., and Coauthors, 2016: The Pale Orange Dot: The Spectrum and Habitability of Hazy Archean Earth. *Astrobiology*, **16 (11)**, 873–899, doi:10.1089/ast.2015.1422, URL https://www.liebertpub.com/doi/full/10.1089/ast.2015.1422, publisher: Mary Ann Liebert, Inc., publishers.

Blake, R. E., S. J. Chang, and A. Lepland, 2010: Phosphate oxygen isotopic evidence for a temperate and biologically active Archaean ocean. *Nature*, **464 (7291)**, 1029–1032, doi: 10.1038/nature08952, URL https://www.nature.com/articles/nature08952, publisher: Nature Publishing Group.

Brenner, S., L. Rainville, J. Thomson, S. Cole, and C. Lee, 2021: Comparing Observations and Parameterizations of Ice-Ocean Drag Through an Annual Cycle Across the Beaufort Sea. *Journal of Geophysical Research: Oceans*, **126 (4)**, e2020JC016 977, doi:10.1029/2020JC016977, URL https://onlinelibrary.wiley.com/doi/abs/10.1029/2020JC016977, _eprint: https://onlinelibrary.wiley.com/doi/pdf/10.1029/2020JC016977.

Brown, M., T. Johnson, and N. J. Gardiner, 2020: Plate Tectonics and the Archean Earth. *Annual Review of Earth and Planetary Sciences*, **48 (Volume 48, 2020)**, 291–320, doi:10.1146/annurev-earth-081619-052705, URL https://www.annualreviews.org/content/journals/10.1146/annurev-earth-081619-052705, publisher: Annual Reviews.

Brunetti, M., J. Kasparian, and C. Vérard, 2019: Co-existing climate attractors in a coupled aquaplanet. *Climate Dynamics*, **53 (9)**, 6293–6308, doi: 10.1007/s00382-019-04926-7, URL https://doi.org/10.1007/s00382-019-04926-7.

Charnay, B., F. Forget, R. Wordsworth, J. Leconte, E. Millour, F. Codron, and A. Spiga, 2013: Exploring the faint young Sun problem and the possible climates of the Archean Earth with a 3-D GCM. *Journal of Geophysical Research: Atmospheres*, **118 (18)**, 10,414–10,431, doi:10.1002/jgrd.50808, URL https://onlinelibrary.wiley.com/doi/abs/10.1002/jgrd.50808, _eprint: https://onlinelibrary.wiley.com/doi/pdf/10.1002/jgrd.50808.

Covey, C., 1995: Global ocean circulation and equator-pole heat transport as a function of ocean GCM resolution. *Climate Dynamics*, **11 (7)**, 425–437, doi:10.1007/BF00209516, URL https://doi.org/10.1007/BF00209516.

Cullum, J., D. P. Stevens, and M. M. Joshi, 2016: Importance of ocean salinity for climate and habitability. *Proceedings of the National Academy of Sciences*, **113 (16)**, 4278–4283, doi:10.1073/pnas.1522034113, URL https://www.pnas.org/doi/full/10.1073/pnas.1522034113, publisher: Proceedings of the National Academy of Sciences.

de Wit, M. J., and H. Furnes, 2016: 3.5-Ga hydrothermal fields and diamictites in the Barberton Greenstone Belt—Paleoarchean crust in cold environments. *Science Advances*, **2 (2)**, e1500 368, doi:10.1126/sciadv.1500368, URL https://www.science.org/doi/10.1126/sciadv.1500368, publisher: American Association for the Advancement of Science.

Drake, M. J., 2005: Origin of water in the terrestrial planets. *Meteoritics & Planetary Science*, **40 (4)**, 519–527, doi:10.1111/j.1945-5100.2005.tb00960.x, URL https://onlinelibrary.wiley.com/doi/abs/10.1111/j.1945-5100.2005.tb00960.x, _eprint: https://onlinelibrary.wiley.com/doi/pdf/10.1111/j.1945-5100.2005.tb00960.x.

Driese, S. G., M. A. Jirsa, M. Ren, S. L. Brantley, N. D. Sheldon, D. Parker, and M. Schmitz, 2011: Neoarchean paleoweathering of tonalite and metabasalt: Implications for reconstructions of 2.69 Ga early terrestrial ecosystems and paleoatmospheric chemistry. *Precambrian Research*, **189 (1)**, 1–17, doi:10.1016/j.precamres.2011.04.003, URL https://www.sciencedirect.com/science/article/pii/S0301926811000908.

Enderton, D., and J. Marshall, 2009: Explorations of Atmosphere–Ocean–Ice Climates on an Aquaplanet and Their Meridional Energy Transports. *Journal of the Atmospheric Sciences*, **66 (6)**, 1593–1611, doi:10.1175/2008JAS2680.1, URL https://journals.ametsoc.org/view/journals/atsc/66/6/2008jas2680.1.xml, publisher: American Meteorological Society Section: Journal of the Atmospheric Sciences.

Ernst, W. G., 2009: Archean plate tectonics, rise of Proterozoic supercontinentality and onset of regional, episodic stagnant-lid behavior. *Gondwana Research*, **15 (3)**, 243–253, doi:10.1016/j.gr.2008.06.010, URL https://www.sciencedirect.com/science/article/pii/S1342937X0800107X.

Farquhar, J., A. L. Zerkle, and A. Bekker, 2011: Geological constraints on the origin of oxygenic photosynthesis. *Photosynthesis Research*, **107 (1)**, 11–36, doi:10.1007/s11120-010-9594-0, URL https://doi.org/10.1007/s11120-010-9594-0.

Ferreira, D., J. Marshall, and B. Rose, 2011: Climate Determinism Revisited: Multiple Equilibria in a Complex Climate Model. *Journal of Climate*, **24 (4)**, 992–1012, doi:10.1175/2010JCLI3580.1, URL https://journals.ametsoc.org/view/journals/clim/

24/4/2010jcli3580.1.xml, publisher: American Meteorological Society Section: Journal of Climate.

Feulner, G., 2012: The faint young Sun problem. *Reviews of Geophysics*, **50 (2)**, doi:10.1029/2011RG000375, URL https://onlinelibrary.wiley.com/doi/abs/10.1029/2011RG000375, _eprint: https://onlinelibrary.wiley.com/doi/pdf/10.1029/2011RG000375.

Gille, S. T., E. J. Metzger, and R. Tokmakian, 2004: Seafloor topography and ocean circulation. *Oceanography*, doi:10.5670/oceanog.2004.66, URL https://doi.org/10.5670/oceanog.2004.66.

Gough, D. O., 1981: Solar interior structure and luminosity variations. *Solar Physics*, **74 (1)**, 21–34, doi:10.1007/BF00151270, URL https://doi.org/10.1007/BF00151270.

Grist, J. P., S. A. Josey, A. L. New, M. Roberts, T. Koenigk, and D. Iovino, 2018: Increasing Atlantic Ocean Heat Transport in the Latest Generation Coupled Ocean-Atmosphere Models: The Role of Air-Sea Interaction. *Journal of Geophysical Research: Oceans*, **123 (11)**, 8624–8637, doi:10.1029/2018JC014387, URL https://onlinelibrary.wiley.com/doi/abs/10.1029/2018JC014387, _eprint: https://onlinelibrary.wiley.com/doi/pdf/10.1029/2018JC014387.

Kasting, J. F., 2005: Methane and climate during the Precambrian era. *Precambrian Research*, **137 (3)**, 119–129, doi:10.1016/j.precamres.2005.03.002, URL https://www.sciencedirect.com/science/article/pii/S030192680500032X.

Kim, J., S. L. Goldstein, L. D. Pena, M. Jaume-Seguí, K. P. Knudson, M. Yehudai, and L. Bolge, 2021: North Atlantic Deep Water during Pleistocene interglacials and glacials. *Quaternary Science Reviews*, **269**, 107 146, doi:10.1016/j.quascirev.2021.107146, URL https://www.sciencedirect.com/science/article/pii/S027737912100353X.

Kuzmin, M. I., V. V. Yarmolyuk, and R. E. Ernst, 2016: Tectonic activity of the early Earth (4.56-3.4(2.7?) Ga). *Russian Geology and Geophysics*, **57 (5)**, 639–652, doi:10.1016/j.rgg.2016.04.003, URL https://www.sciencedirect.com/science/article/pii/S1068797116300323.

Lepot, K., 2020: Signatures of early microbial life from the Archean (4 to 2.5 Ga) eon. *Earth-Science Reviews*, **209**, 103 296, doi:10.1016/j.earscirev.2020.103296, URL https://www.sciencedirect.com/science/article/pii/S0012825220303421.

Marshall, J., A. Adcroft, C. Hill, L. Perelman, and C. Heisey, 1997a: A finite-volume, incompressible Navier Stokes model for studies of the ocean on parallel computers. *Journal of Geophysical Research: Oceans*, **102 (C3)**, 5753–5766, doi:10.1029/96JC02775, URL https://onlinelibrary.wiley.com/doi/abs/10.1029/96JC02775, _eprint: https://onlinelibrary.wiley.com/doi/pdf/10.1029/96JC02775.

Marshall, J., D. Ferreira, J.-M. Campin, and D. Enderton, 2007: Mean Climate and Variability of the Atmosphere and Ocean on an Aquaplanet. *Journal of the Atmospheric Sciences*, **64 (12)**, 4270–4286, doi:10.1175/2007JAS2226.1, URL https://journals.ametsoc.org/view/journals/atsc/64/12/2007jas2226.1.xml, publisher: American Meteorological Society Section: Journal of the Atmospheric Sciences.

Marshall, J., C. Hill, L. Perelman, and A. Adcroft, 1997b: Hydrostatic, quasi-hydrostatic, and nonhydrostatic ocean modeling. *Journal of Geophysical Research: Oceans*, **102 (C3)**, 5733–5752, doi:10.1029/96JC02776, URL https://onlinelibrary.wiley.com/doi/abs/10.1029/96JC02776, _eprint: https://onlinelibrary.wiley.com/doi/pdf/10.1029/96JC02776.

Marty, B., G. Avice, D. V. Bekaert, and M. W. Broadley, 2018: Salinity of the Archaean oceans from analysis of fluid inclusions in quartz. *Comptes Rendus. Géoscience*, **350 (4)**, 154–163, doi:10.1016/j.crte.2017.12.002, URL https://comptes-rendus.academie-sciences.fr/geoscience/articles/10.1016/j.crte.2017.12.002/.

Mercier, H., G. L. Weatherly, and M. Arhan, 2000: Bottom water throughflows at the Rio de Janeiro and Rio Grande Fracture Zones. *Geophysical Research Letters*, **27 (10)**, 1503–1506, doi:10.1029/2000GL011402, URL https://onlinelibrary.wiley.com/doi/abs/10.1029/2000GL011402, _eprint: https://onlinelibrary.wiley.com/doi/pdf/10.1029/2000GL011402.

Muilwijk, M., T. Hattermann, T. Martin, and M. A. Granskog, 2024: Future sea ice weakening amplifies wind-driven trends in surface stress and Arctic Ocean spin-up. *Nature Communications*, **15 (1)**, 6889, doi:10.1038/s41467-024-50874-0, URL https://www.nature.com/articles/s41467-024-50874-0, publisher: Nature Publishing Group.

Olson, S., M. F. Jansen, D. S. Abbot, I. Halevy, and C. Goldblatt, 2022: The Effect of Ocean Salinity on Climate and Its Implications for Earth's Habitability. *Geophysical Research Letters*, **49 (10)**, e2021GL095 748, doi:10.1029/2021GL095748, URL https://onlinelibrary.wiley.com/doi/abs/10.1029/2021GL095748, _eprint: https://onlinelibrary.wiley.com/doi/pdf/10.1029/2021GL095748.

Piani, L., and Coauthors, 2023: Hydrogen Isotopic Composition of Hydrous Minerals in Asteroid Ryugu. *The Astrophysical Journal Letters*, **946 (2)**, L43, doi: 10.3847/2041-8213/acc393, URL https://dx.doi.org/10.3847/2041-8213/acc393, publisher: The American Astronomical Society.

Rippeth, T. P., and E. C. Fine, 2022: Turbulent Mixing in a Changing Arctic Ocean. *Oceanography*, **35 (3/4)**, 66–75, URL https://www.jstor.org/stable/27182697, publisher: Oceanography Society.

Roberts, M. J., and Coauthors, 2020: Sensitivity of the Atlantic Meridional Overturning Circulation to Model Resolution in CMIP6 HighResMIP Simulations and Implications for Future Changes. *Journal of Advances in Modeling Earth Systems*, **12 (8)**, e2019MS002 014, doi:10.1029/2019MS002014, URL https://onlinelibrary.wiley.com/doi/abs/10.1029/2019MS002014, _eprint: https://onlinelibrary.wiley.com/doi/pdf/10.1029/2019MS002014.

Rose, B. E. J., 2015: Stable “Waterbelt” climates controlled by tropical ocean heat transport: A nonlinear coupled climate mechanism of relevance to Snowball Earth. *Journal of Geophysical Research: Atmospheres*, **120 (4)**, 1404–1423, doi:10.1002/2014JD022659, URL https://onlinelibrary.wiley.com/doi/abs/10.1002/2014JD022659, _eprint: https://onlinelibrary.wiley.com/doi/pdf/10.1002/2014JD022659.

Sagan, C., and G. Mullen, 1972: Earth and Mars: Evolution of Atmospheres and Surface Temperatures. *Science*, **177 (4043)**, 52–56, doi:10.1126/science.177.4043.52, URL https://www.science.org/doi/10.1126/science.177.4043.52, publisher: American Association for the Advancement of Science.

Smith, R. S., C. Dubois, and J. Marotzke, 2006: Global Climate and Ocean Circulation on an Aquaplanet Ocean–Atmosphere General Circulation Model. *Journal of Climate*, **19 (18)**, 4719–4737, doi:10.1175/JCLI3874.1, URL https://journals.ametsoc.org/view/journals/clim/19/18/jcli3874.1.xml, publisher: American Meteorological Society Section: Journal of Climate.

Som, S. M., R. Buick, J. W. Hagadorn, T. S. Blake, J. M. Perreault, J. P. Harnmeijer, and D. C. Catling, 2016: Earth's air pressure 2.7 billion years ago constrained to less than half of modern levels. *Nature Geoscience*, **9 (6)**, 448–451, doi:10.1038/ngeo2713, URL https://www.nature.com/articles/ngeo2713, publisher: Nature Publishing Group.

Trenberth, K. E., and J. M. Caron, 2001: Estimates of Meridional Atmosphere and Ocean Heat Transports. URL https://journals.ametsoc.org/view/journals/clim/14/16/1520-0442_2001_014_3433_eomaao_2.0.co_2.xml, section: Journal of Climate.

Way, M. J., and Coauthors, 2017: Resolving Orbital and Climate Keys of Earth and Extraterrestrial Environments with Dynamics (ROCKE-3D) 1.0: A General Circulation Model for Simulating the Climates of Rocky Planets. *The Astrophysical Journal Supplement Series*, **231 (1)**, 12, doi:10.3847/1538-4365/aa7a06, URL https://dx.doi.org/10.3847/1538-4365/aa7a06, publisher: The American Astronomical Society.

Williams, G. E., 2000: Geological constraints on the Precambrian history of Earth's rotation and the Moon's orbit. *Reviews of Geophysics*, **38 (1)**, 37–59, doi:10.1029/1999RG900016, URL https://onlinelibrary.wiley.com/doi/abs/10.1029/1999RG900016, _eprint: https://onlinelibrary.wiley.com/doi/pdf/10.1029/1999RG900016.

Wolf, E., and O. Toon, 2013: Hospitable Archean Climates Simulated by a General Circulation Model. *Astrobiology*, **13 (7)**, 656–673, doi:10.1089/ast.2012.0936, URL https://www.liebertpub.com/doi/10.1089/ast.2012.0936, publisher: Mary Ann Liebert, Inc., publishers.

Wolf, E., and O. Toon, 2014: Controls on the Archean Climate System Investigated with a Global Climate Model. *Astrobiology*, **14 (3)**, 241–253, doi:10.1089/ast.2013.1112, URL https://www.liebertpub.com/doi/10.1089/ast.2013.1112, publisher: Mary Ann Liebert, Inc., publishers.

Wu, X., K. A. Reed, C. L. P. Wolfe, G. M. Marques, S. D. Bachman, and F. O. Bryan, 2021: Coupled Aqua and Ridge Planets in the Community Earth System Model. *Journal of Advances in Modeling Earth Systems*, **13 (4)**, e2020MS002 418, doi:10.1029/2020MS002418, URL https://onlinelibrary.wiley.com/doi/abs/10.1029/2020MS002418, _eprint: https://onlinelibrary.wiley.com/doi/pdf/10.1029/2020MS002418.

Zahnle, K., M. Claire, and D. Catling, 2006: The loss of mass-independent fractionation in sulfur due to a Palaeoproterozoic collapse of atmospheric methane. *Geobiology*, **4 (4)**, 271–283, doi:10.1111/j.1472-4669.2006.00085.x, URL https://onlinelibrary.wiley.com/doi/abs/10.1111/j.1472-4669.2006.00085.x, _eprint: https://onlinelibrary.wiley.com/doi/pdf/10.1111/j.1472-4669.2006.00085.x.

Zahnle, K. J., M. Gacesa, and D. C. Catling, 2019: Strange messenger: A new history of hydrogen on Earth, as told by Xenon. *Geochimica et Cosmochimica Acta*, **244**, 56–85, doi:10.1016/j.gca.2018.09.017, URL https://www.sciencedirect.com/science/article/pii/S0016703718305349.

Zhang, Y., T. Huck, C. Lique, Y. Donnadieu, J.-B. Ladant, M. Rabineau, and D. Aslanian, 2020: Early Eocene vigorous ocean overturning and its contribution to a warm Southern Ocean. *Climate of the Past*, **16 (4)**, 1263–1283, doi:10.5194/cp-16-1263-2020, URL https://cp.copernicus.org/articles/16/1263/2020/, publisher: Copernicus GmbH.

Zhang, Y., and Coauthors, 2022: Early Eocene Ocean Meridional Overturning Circulation: The Roles of Atmospheric Forcing and Strait Geometry. *Paleoceanography and Paleoclimatology*, **37 (3)**, e2021PA004 329, doi:10.1029/2021PA004329, URL https://onlinelibrary.wiley.com/doi/abs/10.1029/2021PA004329, _eprint: https://onlinelibrary.wiley.com/doi/pdf/10.1029/2021PA004329.